3. SCANNING TUNNELING MICROSCOPY

JIN-FENG JIA, WEI-SHENG YANG, AND QI-KUN XUE

1. BASIC PRINCIPLES OF SCANNING TUNNELING MICROSCOPY

In spite of its conceptually simple operation principle, scanning tunneling microscope (STM) can resolve local electronic structures on an atomic scale in real space on virtually any kind of conducting solid surface under various environments, with little damage or interference to the sample [1]. It has been invented for more than 20 years. Over the years, the STM has been proved to be an extremely versatile and powerful technique for many disciplines in condensed matter physics, chemistry, material science, and biology. In addition, STM can be used as a nano-tool for nano-scale fabrication, manipulation of individual atoms and molecules, and for building nanometer scale devices one atom/molecule at a time.

STM was originally developed to image the topography of surfaces by Binnig and Rohrer in 1982 [1]. For this great invention, they were awarded the Nobel Prize in Physics in 1986. The principle of STM is very simple, in which electron tunneling is used as the mechanism to probe a surface. In the following, in order to understand the operation principle of STM, we first give a brief introduction to the electron tunneling phenomenon.

1.1. Electronic Tunneling

Tunneling phenomena have been studied for long time and can be well understood in terms of quantum theory. As shown in Fig. 1, considering an one-dimensional vacuum barrier between two electrodes (the sample and the tip) and assuming their

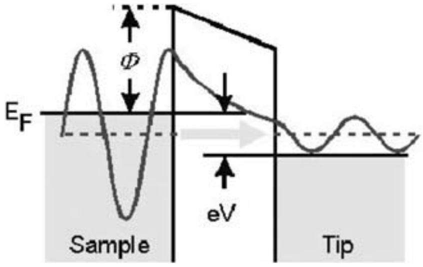

Figure 1. A one dimensional barrier between two metal electrodes. A bias voltage of V is applied between the electrodes.

work functions to be the same and thus the barrier height to be Φ, if a bias voltage of V is applied between the two electrodes with a barrier width d, according to quantum theory under first-order perturbation [2], the tunneling current is

$$I = \frac{2\pi e}{\hbar} \sum_{\mu,\nu} f(E_\mu)[1 - f(E_\nu + eV)]|M_{\mu\nu}|^2 \, \delta(E_\mu - E_\nu), \tag{1}$$

where $f(E)$ is the Fermi function, $M_{\mu\nu}$ is the tunneling matrix element between states ψ_μ and ψ_ν of the respective electrodes, E_μ and E_ν are the energies of ψ_μ and ψ_ν, respectively. Under assumptions of small voltage and low temperature, the above formula can be simplified to

$$I = \frac{2\pi}{\hbar} e^2 V \sum_{\mu,\nu} |M_{\mu\nu}|^2 \, \delta(E_\nu - E_F)\delta(E_\mu - E_F). \tag{2}$$

Bardeen [2] showed that under certain assumptions, the tunneling matrix element can be expressed as

$$M_{\mu\nu} = \frac{\hbar^2}{2m} \int d\vec{S} \cdot (\psi_\mu{}^* \vec{\nabla} \psi_\nu - \psi_\nu{}^* \vec{\nabla} \psi_\mu), \tag{3}$$

where the integral is over all the surfaces surrounding the barrier region. To estimate the magnitude of $M_{\mu\nu}$, the wave function of the sample ψ_ν can be expanded in the generalized plane-wave form

$$\psi_\nu = \Omega_s^{-1/2} \sum_G a_G \exp\left[(k^2 + |\vec{k}_G|^2)^{1/2} z\right] \exp(i\vec{k}_G \cdot \vec{x}), \tag{4}$$

where Ω_s is the volume of the sample, $k = \hbar^{-1}(2m\phi)^{1/2}$ is the decay rate, ϕ is the work function, $\vec{k}_G = \vec{k}_{||} + \vec{G}$, $\vec{k}_{||}$ is the surface component of Bloch vector, and $\vec{G}$ is the surface reciprocal vector.

To calculate the tunneling current, it is necessary to know the tip wave function. Unfortunately, the actual atomic structure of the tip is unknown and, moreover, it is

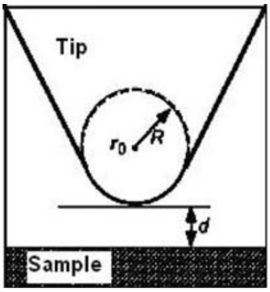

Figure 2. An ideal model for STM tip. The cusp of the tip is assumed to be a sphere with radius of R, the distance from the sample is d, the position of the center of the sphere is $\vec{r}_0$ (From Ref. 3).

very difficult to calculate the tip wave function due to its very low symmetry. However, for the tip we may adopt the reasonable model shown in Fig. 2, which was used by Tersoff *et al.* [3] to describe an ideal tip, and then the wave function of the tip is

$$\psi_\mu = \Omega_t^{-1/2} c_t k R e^{kR} (k|\vec{r} - \vec{r}_0|)^{-1} e^{-k|\vec{r} - \vec{r}_0|}, \tag{5}$$

where Ω_t is the volume of the tip, c_t is a constant determined by the sharpness of the tip and its electronic structure. For simplicity, only the s-wave function of the tip is used in the calculation. Because of

$$(k\vec{r})^{-1} e^{-k\vec{r}} = \int d^2 q b(\vec{q}) \exp\left[-(k^2 + q^2)^{1/2} |z|\right] \exp(i\vec{q} \cdot \vec{x}), \tag{6}$$

$$b(q) = (2\pi)^{-1} k^{-2} (1 + q^2/k^2)^{-1/2}, \tag{7}$$

substituting these wave functions to Eq. (3), we obtain

$$M_{\mu\nu} = \frac{\hbar^2}{2m} 4\pi k^{-1} \Omega_t^{-1/2} k R e^{kR} \psi_\nu(\vec{r}_0), \tag{8}$$

where $\vec{r}_0$ is the position of the cusp center. Substitute Eq. (8) to Eq. (2), we obtain

$$I = 32\pi^3 \hbar^{-1} e^2 V \phi^2 D_t(E_F) R^2 k^{-4} e^{2kR} \sum_\nu |\psi_\nu(r_0)|^2 \delta(E_\nu - E_F), \tag{9}$$

where $D_t(E_F)$ is the density of states at the Fermi level for the tip. Substituting the typical values for metals in Eq. (9), the tunneling current is obtained

$$I \propto V D_t(E_F) e^{2kR} \rho(r_0, E_F), \tag{10}$$

$$\rho(r_0, E_F) = \sum |\psi_\nu(r_0)|^2 \delta(E_\nu - E_F), \tag{11}$$

Thus, the STM with an s-wave tip would simply measure $\rho(r_0, E_F)$, which is the local density of states (DOS) at the Fermi level E_F and at a position r_0, the curvature

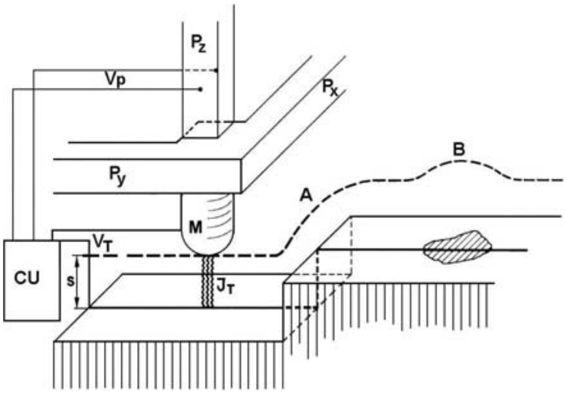

Figure 3. Operation principle of the STM (not to scale). Piezodrives P_X and P_Y scan the metal tip over the surface. The control unit (CU) applies the necessary voltage Vp to piezodrive P_Z to maintain constant tunnel current J_T at bias voltage V_T. The broken line indicates the z displacement in a scan over a surface step (A) and a chemical inhomogeneity (B). (From Ref. 1)

center of the effective tip. Tersoff *et al.* [3] also discussed the contribution of the tip wave function components of higher angular momentum, and found that these just made little difference for typical STM images. So, what the STM measures is only the property of the surface.

Because $|\psi_\nu(\vec{r}_0)|^2 \propto e^{-2k(R+d)}$, thus $I \propto e^{-2kd}$. This means that the tunneling current depends on the tunneling gap distance d very sensitively. In the typical case, the tunneling current would change one order while the gap distance changes only 1 Å. This accounts for extremely high vertical resolution of 0.1 Å of STM.

1.2. Scanning Tunneling Microscope

In March 1981, Binnig, Rohrer, Gerber and Weibel at the IBM Zürich Research Laboratory successfully combined vacuum tunneling with scanning capability, and developed the first STM in the world [1]. The basic idea behind STM is illustrated in Fig. 3. A sharp metal tip is fixed on the top of a pizeodrive (P_Z) to control the height of the tip above a surface. When the tip is brought close enough to the sample surface, electrons can tunnel through the vacuum barrier between tip and sample. Applying a bias voltage on the sample, a tunneling current can be measured through the tip, which is extremely sensitive to the distance between the tip and the surface as discussed above. Another two pizeodrives (P_X and P_Y) are used to scan the tip in two lateral dimensions. A feedback controller is employed to adjust the height of the tip to keep the tunneling current constant. During the tip scanning on the surface, the height of the tip (the voltage supplied to P_Z pizeodrive) is recorded as an STM image, which represents the topograph of the surface. This operation mode of STM is called "constant current" mode.

Constant current mode is mostly used in STM topograph imaging. It is safe to use the mode on rough surfaces since the distance between the tip and sample is adjusted by the feedback circuit.

On a smooth surface, it is also possible to keep the tip height constant above the surface, then, the variation of the tunneling current reflects the small atomic corrugation of the surface. This "constant height" mode has no fundamental difference to the "constant current" mode. However, the tip could be crashed if the surface corrugation is big. On the other hand, the STM can scan very fast in this mode for research of surface dynamic processes.

To achieve the atomic resolution, there are many requirements in STM design and instrumentation, *e.g.*, vibration isolation, scanning devices, positioning devices, electronic controller system *etc.* The details about STM design and instrumentation can be found in many review books [4–6] and will not be discussed here.

STM is so powerful that numerous researches have been done in various scientific areas since its invention. In the following sections, some representative and important applications of STM will be shown and discussed. According to the main functions of STM, the applications can be classified into three parts, *e.g.*, surface imaging, tunneling spectroscopy, and tip manipulation. In the last part, the current development in STM will also be introduced.

2. SURFACE STRUCTURE DETERMINATION BY SCANNING TUNNELING MICROSCOPY

As a microscope, STM can provide very high resolution images in real-space. These images can be used to investigate surface structures, and also surface or even subsurface atomic dynamic processes.

Before the STM was invented, surface structures were very difficult to be determined by conventional surface analysis techniques, such as low-energy electron diffraction (LEED), reflected high-energy electron diffraction (RHEED) and X-ray diffraction *etc.* Besides, these traditional techniques focus essentially only on average or collective properties. The ability to reveal the local surface atomic structure in real space make the STM very fruitful in the field of surface science, especially for structure determination.

2.1. Semiconductor Surfaces

2.1.1. Element Semiconductors

Silicon is the most important material in semiconductor industry. The 7 × 7 reconstruction of the Si(111) surface was first observed by Schlier and Farnsworth [7] with LEED in 1959. After then, all surface sensitive techniques have been used to determine its atomic structure, and a lot of models have been proposed to understand this complicated surface. Due to its large unit cell (49 times of the bulk unit cell), to determine its structure was a great challenge for traditional methods.

The first atomically resolved STM image of this surface was obtained by Binnig *et al.* in 1982, which marks a breakthrough in the study of Si(111)7 × 7 and also in the development of STM itself [1], because it was also the first atomically resolved image

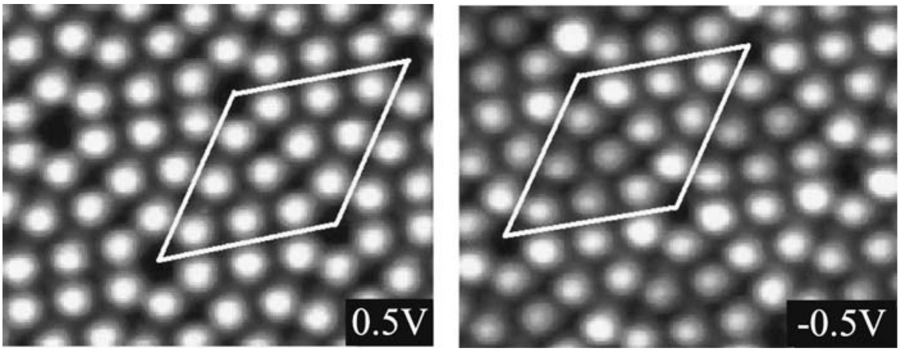

Figure 4. Atomically resolved STM images of the Si(111)7 × 7 surface. Bias voltage: +0.5 V (left), −0.5 V (right). A unit cell is outlined in the images, the size of the unit cell is 2.7 nm × 2.7 nm.

provided by STM. From then, the surface has been extensively studied with STM. As shown in Fig. 4, the STM images of Si(111)7 × 7 reveal 12 protrusions in each unit cell, and the negative biased STM image clearly shows the inequivalence between the adatoms in the two halves of a unit cell. And also, there is a corner hole in each unit cell. The information immediately helped to rule out many models proposed at that time.

The structure was finally determined by Takayanagi *et al.* in 1985 [8] on the basis of transmission electron diffraction data. The dimer-adatom-stacking-fault (DAS) model proposed by Takayanagi *et al.* is shown in Fig. 5. In the DAS model a 7 × 7 unit cell consists of 12 adatoms, 9 dimers, 6 rest atoms, and a corner hole. The atomic layers in the right triangle (or half) of the unit cell are stacked regularly and thus this half is called as unfaulted half unit cell (UFHUC), while the left half contains a stacking-fault and thus is called as fault half unit cell (FHUC), see Fig. 5(b).

For the truncated Si(111)1 × 1 surface, each surface Si atom has a dangling bond, which contribute significantly to the total surface energy. To reduce the total surface energy, the surface reconstructs to 7 × 7 and the number of dangling bond decrease from 49 to 19 per unit cell. In the DAS model, each adatom reduces 2 dangling bonds by saturating 3 dangling bonds and leading to a single dangling bond due to the fourfold coordination of Si atom. The other 7 dangling bonds are located on the 6 rest atoms and the atom at the bottom of the corner hole. The DAS model can explain the images very well. Since the dangling bonds on the adatom are partially filled, each adatom is imaged as a bright protrusion at both positive and negative biases. The inequivalence between the adatoms in two different triangles in the negatively biased STM images can be explained by the slight electronic difference caused by the stacking-fault.

In many cases, STM could not be used solely to determine surface structure since it probes only the structural information of the topmost surface layer. Moreover, it generally lacks chemical specificity. Below, we can see that the mixed topographic and

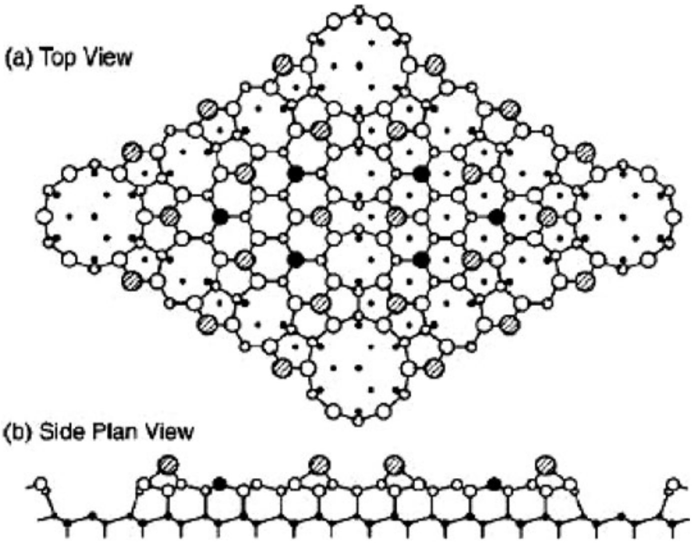

Figure 5. Top (a) and side (b) views of the dimer-adatom-stacking-fault (DAS) model of the Si(111)7 × 7 surface. The large striped circles designate the adatoms, the large solid circles designate the rest atoms, the large and small open circles the Si atoms in the 2nd and 3rd bilayers, and the small solid circles the atoms in 4th and 5th bilayer, respectively. (Proposed by Takayanagi *et al.*)

electronic features cause difficulties to determine atomic structures by STM. For this purpose, it is very important to combine STM with other relative techniques.

2.1.2. Compound Semiconductors

GaAs is a very important compound semiconductor since many electronic and optoelectronic devices are made of it. Because of its zincblend crystal structure with a tetrahedral coordination in the bulk, the polar GaAs(001) surface could be terminated with either As or Ga atoms. As a function of growth temperature, As/Ga flux ratio and preparation conditions, the (001) surface displays a number of reconstructions, starting with the most As-rich phase which has a c(4 × 4) symmetry, through the 2 × 4/c(2 × 8), 2 × 6, 4 × 6, ending with the 4 × 2/c(8 × 2) Ga-stabilized phase.

Among them, the As-rich 2 × 4 phases are the most important structures commonly used in the technological applications. It is generally accepted that the top layer of the As-rich 2 × 4 phase consists of As dimers [9]. Farrell and Palmstron analyzed their experimental results for the 2 × 4 phase and classified them into three (α, β, and γ) phases depending on the RHEED spot intensities [10]. According to different experiments, many structure models were proposed for each phase [11, 12]. Four different models are shown in Fig. 6. To solve the controversy, Hashizume *et al.* performed a comprehensive study on the surface with STM and RHEED [13, 14]. The typical STM images together with atomic resolved zoom-in images and line profiles along [110] direction are shown in Fig. 7. From the atomic resolved STM images, they

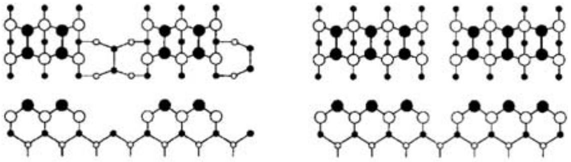

(a) Bilayer two-As-dimers model

(b)Three As dimer model

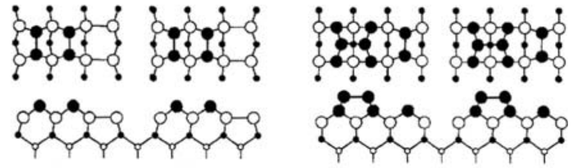

(c)two As-dimer model with second layer Ga dimerrized

(d)extra-As dimer model

Figure 6. Four structure models proposed for the GaAs(001) 2 × 4 reconstruction. Filled (open) circles denote As (Ga) atoms. (From Ref. 13)

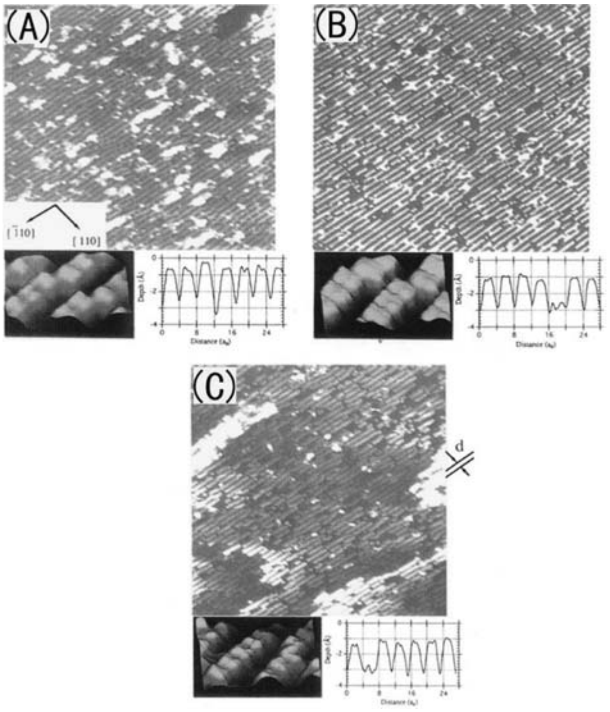

Figure 7. Typical STM images (800 Å × 800 Å) of the (A) α, (B) β and (C) γ phases together with the zoom-in images and line profiles along [110] direction of the GaAs(001) 2 × 4 reconstruction. (From Ref. 13)

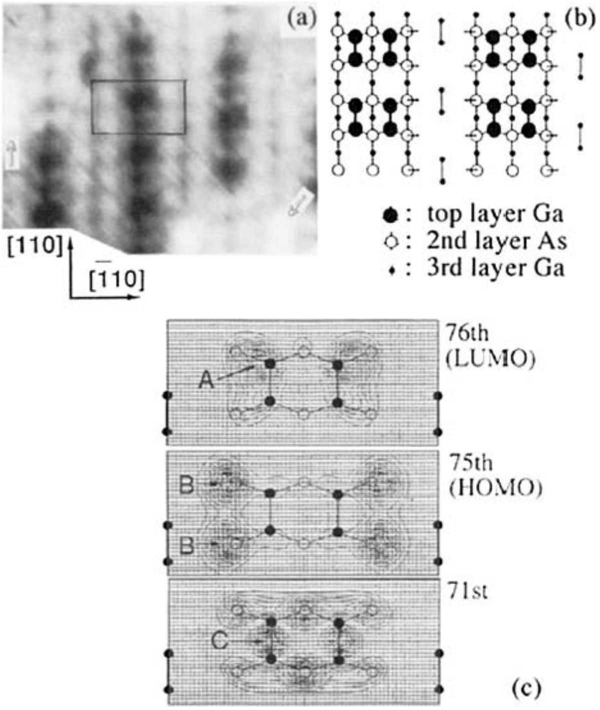

Figure 8. (a) Atomic resolution filled state STM image of the GaAs(001) 4 × 2 phase. (b) The Ga-dimer-model for 4 × 2 phase. (c) The charge distributions of the local density of the states calculated based on the Ga-model in (b) at 0.9 Å above the first layer Ga-dimer position for the 76 (LUMO), 75th (HOMO) and 71st bands. (From Ref. 15)

concluded that the outermost surface layer of the unit cell of the 2 × 4 α, β, and γ phases all consists of two As dimers and that the α and β phases are different in the atomic arrangements of the second and third layers exposed by the dimer vacancy rows. The γ phase is the less ordered β phase with "open areas" exposing the underneath disordered c(4 × 4) phase. To fully understand the structures of the α, β, and γ phases, the RHEED spot intensities for the possible 2 × 4 models were calculated using the dynamical theory. According to the calculations, they proposed a unified model: the two As-dimer model by Chadi [11] (Fig. 6a) for the most stable β phase, and the two As-dimer model incorporated with the relaxation of the second layer Ga atoms proposed by Northrup and Froyen [12] (Fig. 6c) for α phase, while the γ phases is the locally ordered β phase with the disordered c(4 × 4) unit in the open area [13].

For the GaAs(001) Ga-rich 4 × 2/c(2 × 8) and 4 × 6 phases, *Xue et al.* performed a systematical investigation with an MBE-STM system [15]. Fig. 8 shows the high-resolution filled-state STM images of the 4 × 2 surface. The 4 × 2 unit cells are highlighted in the STM images. In the filled state image, a pair of rows separated by 5.1 Å along the [−110] direction is observed, whereas the row itself is a chain of bright protrusions separated by 4 Å along the [110] direction. A new finding here is faintly imaged features which are located in the outskirt of the paired row. The weak features always couple together to form a pair-like structure in parallel to the bright rows. The separation between the neighboring pair-like features along the [110] direction was determined to be 8 Å, resulting in the 4 × 2 symmetry. The out-of phase arrangement of the 4 × 2 sub-unit gives rise to the c(8 × 2) symmetry.

Several models have been proposed for this phase, however, none of them can explain the observed STM images straightforwardly since the overlapping first layer Ga and the second layer As orbits are both accessible to the STM in the range of applied negative bias voltage to the sample and the STM is probing the local density of states near the Fermi level, not merely the surface geometry [15]. In order to resolve this discrepancy, first-principles total energy calculations of the surface charge density distribution based on the Ga-bilayer model (see Fig. 8(b)) have been performed. The calculated results are shown in Fig. 8(c). Under the filled states STM imaging condition at −1.8 V, it is found that all local densities of the states between the 71st and the 76th bands contribute to the tunneling current to form the STM image [Fig. 8(a)]. Because of the smaller potential barrier height for tunneling from the 75th band, the 75th HOMO makes the most significant contribution to the tunneling together with contributions from the overlapping 74th, 73rd and 72nd bands with the decreasing contribution, all of which are basically imaging of the second layer As atoms as individual brighter protrusions. On the other hand, the contribution for the top layer Ga dimer becomes only appreciable down at the 71st band at the middle of the Ga dimer. Thus, the top layer Ga dimer is observed as single faint hump (instead of pair-like feature) even though they are located in the top layer. Thus, the calculated results agree with the STM observation well.

Very recently, this surface was studied by theory and other techniques. A different model (called as $\zeta(4 \times 2)$) was proposed by Lee, Moritz, and Scheffler, as shown in Fig. 8(d) [16]. This model well explains the STM images, particularly the empty state image. Later, more theories and experiments support this model [17]. But, regarding to the significant rearrangement of the surface atoms, more evidences are needed to justify the model.

The Ga-rich 4 × 6 phase can be obtained by a higher Ga flux ratio in migration enhanced epitaxy or annealing the 2 × 6 phase for longer time (>15 mins) [15]. An atomic resolved STM image of 4 × 6 reconstruction is shown in Fig. 9, which is uniquely characterized by the array of large oval protrusions regularly located at each corner of the unit cell. The oval features are ~0.1 Å higher than the Ga dimers. By compared the image with the Fig. 8, it was concluded that the pair of bright rows running in the [110] direction in Fig. 9 is the first layer Ga-dimers, instead of second layer As atoms, unlike in the case of 4 × 2 phase. The large bright oval features occupy the middle of the As rows, by overlapping with them. In Fig. 9, every individual Ga dimer is clearly resolved. Such high contrast imaging of the Ga dimers is likely due to charge transfer from the oval protrusions to the Ga dimers. After careful analysis, Xue *et al.* concluded

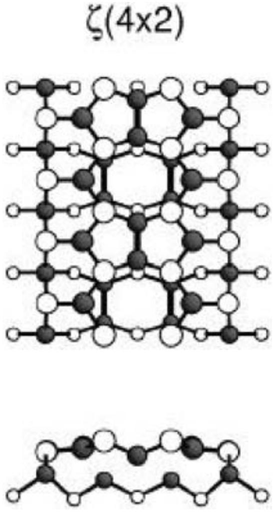

Figure 8. (d) Top views (upper row) and side views (lower row) of the $\zeta(4 \times 2)$ structure of Ga-rich GaAs(001)-4 × 2 surface. Solid spheres denote Ga atoms and open spheres As atoms. The sphere sizes reflect the distance from the surface. Dimer bonds are marked by thicker lines. (From Ref. 16)

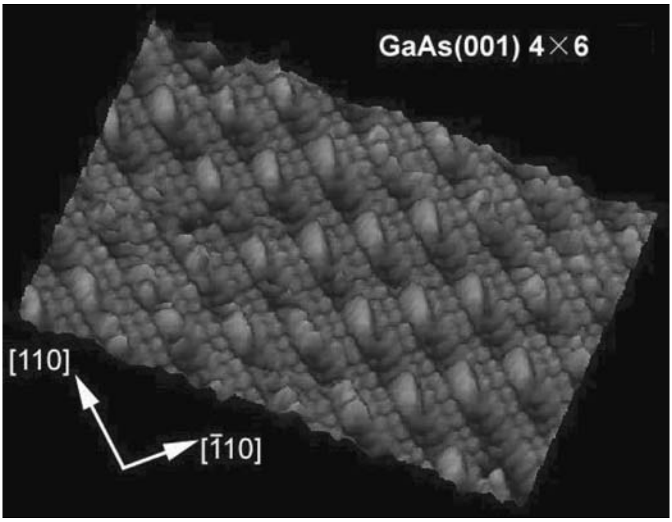

Figure 9. Atomic resolved STM image of GaAs(001) 4 × 6 surface obtained with $V_b = -1.8$ V and $I_t = 40$ pA. (From Ref. 15)

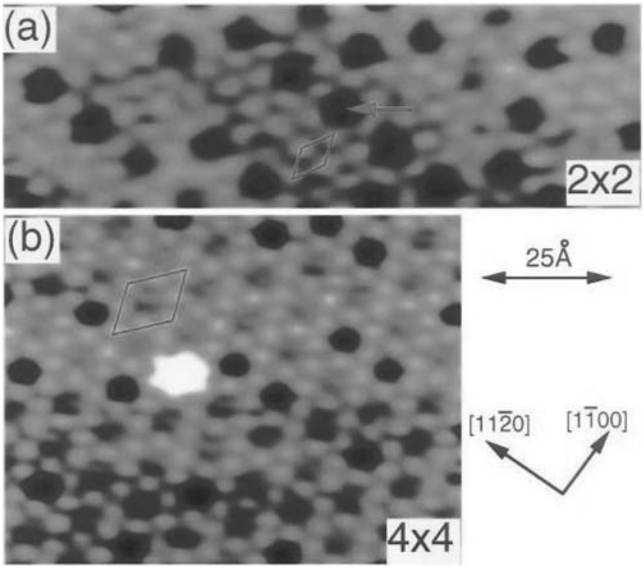

Figure 10. Filled states STM images showing (a) 2 × 2 phase (at −3.0 V), (b) 4 × 4 phase (at −2.8 V). The red arrow in (a) depicts a missing 2 × spot which transfers the 2 × 2 into the 4 × 4 structure. (From Ref. 21)

that the Ga-rich 4 × 6 phase accommodates the periodic array of Ga clusters at the 4 × 6 unit corner on top of the 4 × 2 phase. Further theoretical study does not seem to support the model, and thus the nature of the big oval protrusion keep unresolved [17].

Wide band-gap III–V nitrides (Ga/In/Al/N) have attracted much interest because of their enormous applications in short wavelength optoelectronic devices [18–21]. Absence of reversion symmetric center in hexagonal GaN crystal gives rise to a freedom in its thin film polarity; the (0001) polar surface terminated with a Ga-N bilayer known as the Ga polarity and the (000$\bar{1}$) polar surface terminated with a N-Ga bilayer known as the N polarity [20]. As the present device application depends on controlled heteroepitaxy of the GaN thin film, which is essentially a surface process, complete knowledge of the surface atomic structure is highly desirable. A study of its surface reconstructions is also of great interest since GaN, a special case of the III–V compound semiconductors, is made up of the species possessing large differences in atom radius, electronegativity, and cohesive energy, and contains both covalent and ionic bonds. GaN is also the only III–V that crystallizes in the hexagonal form [21].

The 2 × 2 and 4 × 4 reconstructions of the Ga-polar GaN(0001) surface have been studied with STM first by Xue *et al.* [21] A typical filled state STM image of the 2 × 2 phase is shown in Fig. 10(a). The 2 × 2 symmetry is evident by a regular array of bright spots separated by 6.4 Å along both the close-packing directions. The Ga-adatom model and the Ga-vacancy model are proposed for this reconstruction. However, the

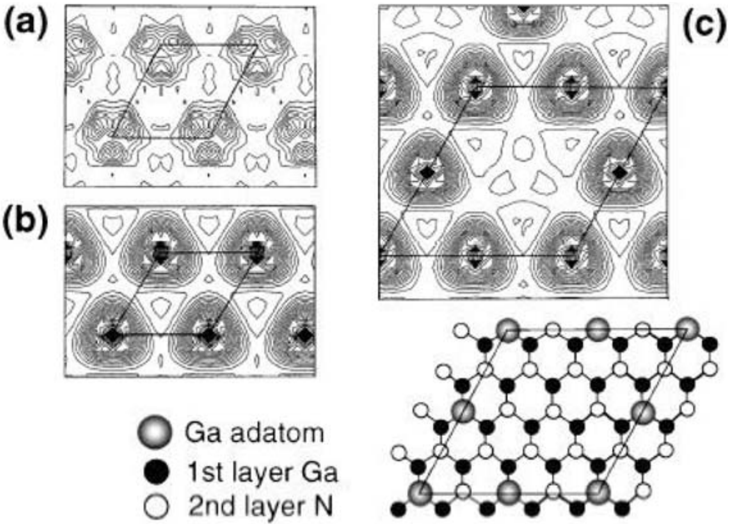

Figure 11. Surface charge density distribution calculated for (a) 2 × 2 Ga-vacancy, (b) 2 × 2 Ga-adatom, and (c) 4 × 4 Ga-adatom models. The local density of states is integrated from the valence bands covering about 2 eV below the highest occupied molecular orbital band, which is cut at 1.3 Å above the outermost surface layer. (From Ref. 21)

correct model cannot be established solely by the STM images. First-principles total-energy calculations again are carried out to resolve this problem [21]. In the charge density calculation, the charge is a sum of valence bands covering a range of about 2 eV below the highest occupied molecular orbital and is a reasonable approach to the STM data (~3 eV). An excellent agreement is obtained for the Ga-adatom model [Fig. 11(b)]. On the other hand, despite an expected coupling of the $2p$ orbits of three threefold coordinated N atoms in the (0001) basal plane, the charge distributions of the Ga-vacancy structure are split spatially [Fig. 11(a)], and do not agree with the experiment.

As for the 4 × 4 phase [Fig. 10(b)], some individual 4 × 4 units are observed due to missing spots from the 2 × 2 phase [as indicated by the arrow in Fig. 10(a)]. During annealing from 200 to 300 °C, the 2 × 2 and 4 × 4 phases always coexist. The change to the 4 × 4 phase with increasing temperature, which results in Ga atom/adatom loss, suggests that the 4 × 4 forms by the Ga desorption from the 2 × 2 surface. A missing adatom model is proposed for the 4 × 4 and investigated it theoretically [Fig. 11(c)]. The agreement between the experiment and theory is excellent [Figs. 10(b) and 11(c)]. Despite this, a model for the 4 × 4 reconstruction containing three As adatoms and one Ga adatom per 4 × 4 cell is present in [22]. Therefore, the correct model for Ga-polar GaN(0001) 4 × 4 structure is still under dispute.

Reconstructions of 2 × 2, 5 × 5, 6 × 4 and pseudo-1 × 1 appeared on Ga-polar GaN(0001) surface were reported by Smith *et al.* [23, 24]. It indicates that the

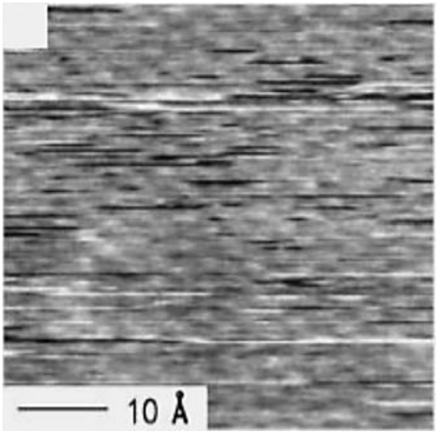

Figure 12. Atomic resolution STM image of pseudo-1 × 1 reconstruction (at −0.25 V) (From Ref. 23)

morphology of GaN(0001) surface will vary with different Ga concentration and substrate temperature. In previous study [23, 24], they showed from total energy calculations that both 2 × 2 N-adatom in H3 site model and 2 × 2 Ga-adatom in T4 site model are more stable where Ga and N adatoms are proposed to bond to three underlying Ga atoms in the Ga terminated Ga-N bilayer. Since the 2 × 2 reconstruction can be obtained by nitriding Ga-polar surface at about 600 °C, they proposed that this reconstruction may be composed of N atoms. Later, they poined out that the 2 × 2 reconstruction results from unintentional contamination of As [25].

Under Ga-rich condition the most stable phase is pseudo-1 × 1 structure, which shows sideband in RHEED pattern and satellite spots in LEED pattern. Pseudo-1 × 1 structure can be obtained either by terminating GaN growth and cooling under 350 °C, or by depositing 2 ∼ 3 ML Ga on the Ga-polar surface and annealing for a period of time. A laterally contracted Ga bilayer model is proposed by Northrup *et al.* [26]. Due to the satellite spots in LEED pattern Ga atoms in pseudo-1 × 1 Ga-bilayer are proposed to experience a rapid moving process. Therefore, the STM image of pseudo-1 × 1 reconstruction is a time-average result which probably indicates the underlying corrugation of GaN(0001) substrate (see Fig. 12).

The 5 × 5 reconstruction can be obtained by the following process: first annealing pseudo-1 × 1 phase at 750 °C, then depositing 1/2 ML Ga and reannealing at 700 °C. The 6 × 4 reconstruction is obtained by depositing 1/2 ML Ga on the 5 × 5 reconstruction and annealing at 700 °C. The 5 × 5 reconstruction and the row-like 6 × 4 reconstruction both depend on the bias voltage as seen in Fig. 13, which were suggested to be semiconducting. For the 5 × 5 reconstruction a structure model that contains Ga adatom in T4 site, N adatom in H3 site and Ga vacancies has been proposed [24].

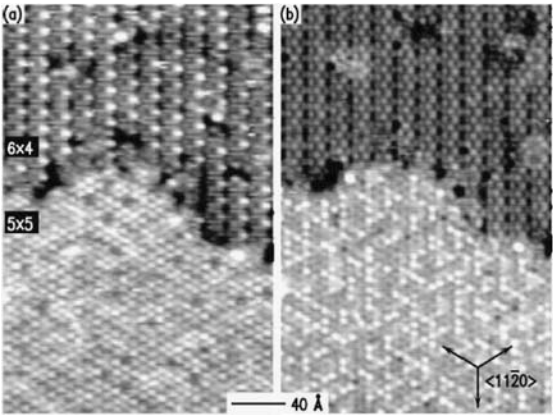

Figure 13. Dual bias images of the 5 × 5 and 6 × 4 reconstructions. The average height difference between the two reconstructions is 0.3 Å for empty states (+1.0 V sample voltage) shown in (a) and 0.4 Å for filled states (−1.0 V sample voltage) shown in (b), with the 5 × 5 being higher in each case. In both images, the total gray scale range is about 1.3 Å. (From Ref. 24)

The adsorption behavior of Ga on Ga-polar GaN(0001) was studied by specular RHEED intensity analysis. It demonstrates that the Ga coverage on GaN(0001) surface during homoepitaxial growth is a function of the Ga flux and the substrate temperature. They divided Ga absorption process into three regions according to the Ga coverage that is flux dependent. The Ga coverage is increased with Ga flux less than 0.20 ML/s. When Ga flux is between 0.20 ML/s and 0.72 Ml/s, the Ga coverage is almost unchangeable. If Ga flux is larger than 0.72 ML/s, Ga droplets form and there will be no finite equilibrium Ga coverage under higher Ga flux. Thus, the transition fluxes vary exponentially with the substrate temperature [27, 28].

Reconstructions of the N-polar GaN(0001) were investigated by STM first by Smith *et al.* [29]. They observed four reconstructions: 1 × 1, 3 × 3, 6 × 6, and c(6 × 12). The 3 × 3, 6 × 6 and c(6 × 12) reconstructions can be obtained by depositing submonolayer Ga atoms on the 1 × 1 structure. The STM images of these reconstructions are shown in Fig. 14. The 1 × 1 reconstruction appears to be hexagonal which has the same lattice to that of GaN. The 3 × 3 reconstruction also shows similar hexagonal arrangement. The 6 × 6 reconstruction displays a ring-like structure. Each ring has threefold symmetry with lobes from three neighboring rings coming close together, which results in two different height "holes" around the rings. The row-like c(6 × 12) reconstruction shows a bias-dependent characteristic, which is different from other reconstructions.

They have proposed the structure models of 1 × 1 and 3 × 3 reconstructions as shown in Fig. 15. The 1 × 1 reconstruction is suggested to contain 1ML Ga atoms bonded to the top N atoms in the N-terminated GaN bilayer. For the 3 × 3 reconstruction, the Ga adatoms are supposed to bond on top of the 1 × 1 Ga adlayer.

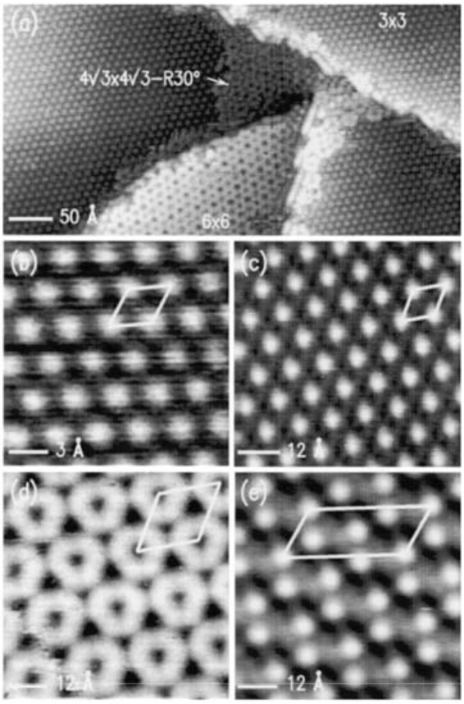

Figure 14. STM images of the N-polar GaN(0001) surface displaying (a) mixed reconstructions, with dislocation near center of image, (b) 1×1, (c) 3×3, (d) 6×6, and (e) $c(6 \times 12)$ reconstructions. Sample bias voltages are +1.0, −0.75, −0.1, +1.5, and +1.0 V, respectively. Tunnel currents are in the range 0.03—0.11 nA. Gray scale ranges are 4.2, 0.17, 0.88, 1.33, and 1.11 Å, respectively. Unit cells are indicated with edges along <1120> directions. (From Ref. 29)

2.1.3. Metal Adsorption on Semiconductors—In Nanoclusters

In the last decade, fabrication and understanding of nanoclusters have become one of the most exciting areas of research. This is driven by their great potential applications in technology and scientific importance to bridge our understanding between molecular and condensed matter physics. Recently, Xue's group explored a method of surface-mediated magic clustering and successfully fabricated the artificial cluster crystals, i.e., the periodical array of identical nanoclusters by using the ordered reconstructed semiconductor surface-the Si(111)-7×7 as a template [30–32].

The STM image of periodical In nanocluster array on Si(111)7×7 is shown in Fig. 16(a). All In nanoclusters are completely identical and also in a perfect ordering since In clusters only occupy the FHUC of Si(111)-7×7. The atomic resolution STM images of the In clusters at different sample biases (+0.5 V, +0.3 V and –0.3 V) are shown in Fig. 16(b)–(d), respectively. In the empty state images, the In clusters appear as hollow-centered six-spot equilateral triangles with a distance between the spots of ~5.0 ± 0.5 Å, which is much larger than the surface lattice constant 3.84 Å of the

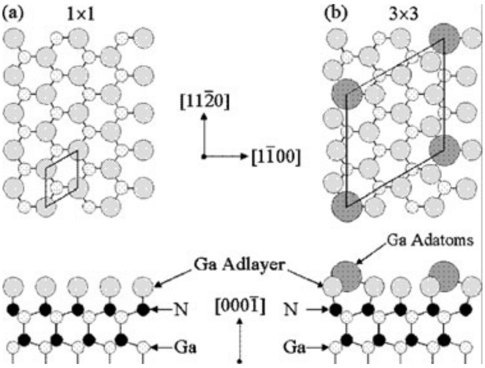

Figure 15. Schematic view of the structures for the (a) 1 × 1 Ga adlayer and (b) 3 × 3 adatom-on-adlayer reconstructions of GaN(0001). For the 3 × 3 structure, the lateral (in-plane) displacement of the adlayer atoms bonded to the Ga adatom is 0.51 Å away from the adatom. All other lateral or vertical displacements of the adlayer atoms are less than 0.1 Å. (From Ref. 29)

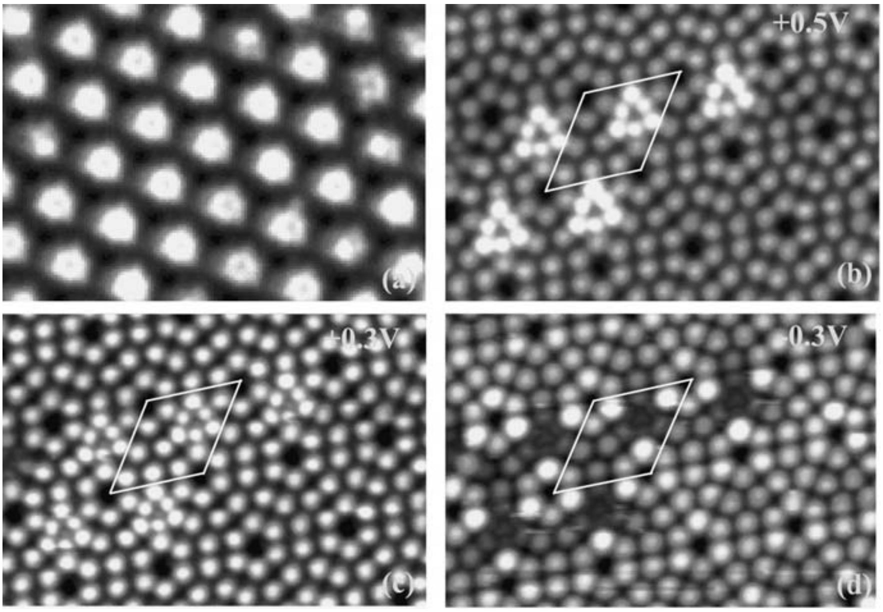

Figure 16. (a) STM image of a periodical In nanocluster array. (b–d) Atomic resolved STM images of In nanoclusters at different bias voltages, showing a pronounced bias voltage dependence of the observed images. (From Ref. 30)

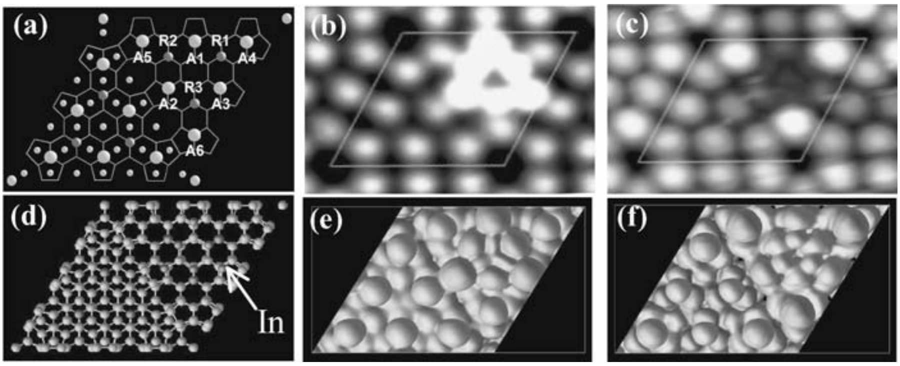

Figure 17. (a) The DAS model of Si(111)-7 × 7 surface. The FHUC is to the upper-right corner. The sites relevant to the discussion are indicated as R1–R3 for Si rest atoms and A1–A6 for Si adatoms. The yellow balls are Si atoms in the substrate, the blue balls are Si adatoms, and the red balls are Si rest atoms. (b) and (c) The STM images of the In clusters recorded at sample bias voltages of +0.6 V and –0.3 V, respectively. (d) Top view of the calculated atomic structure of the six-In cluster on Si(111)-7 × 7. The dark blue balls are In atoms. The calculated STM images are shown in (e) (for positive bias +0.6 V) and (f) (for negative bias at –0.3 V with respect to the Fermi energy) for the atomic structure in (d). The color code indicates the height of the images: dark blue being low and red being high. At typical experimental tip height of about 1 nm above the surface, only the most protruding features can be seen.

Si(111)-1 × 1 and the In-In nearest neighbor distance 3.25 Å. The triangular pattern is quite unusual in terms of normal close-packed structures observed previously. In the filled state images, however, the six-spot equilateral triangles disappear completely and the most protrusive features are the corner adatoms. The strong bias dependence of the images makes it very difficult to deduce the atomic structure of In clusters although it can be concluded that there are six In atoms in each cluster [30].

First-principles total energy calculations are employed to solve the problem. After optimization, the model in Fig. 17(d) is obtained. In this model, the six threefold-coordinated In atoms form a triangle [Fig. 17(d)]. For those In atoms at the corners of the triangle, the bond lengths are 2.57 Å, 2.64 Å, and 2.64 Å, whereas the bond angles are 113°, 113°, and 88°, respectively. For those In atoms on the edges, the bond lengths are 2.67 Å, 2.60 Å, and 2.60 Å, whereas the bond angles are 113°, 116° and 116°, respectively. Angles larger than the 109.5°-tetrahedral angle are preferential as threefold In prefers planar 120° bond angles. Both the three Si adatoms [A1–A3 in Fig. 17(a)] and the three Si rest atoms [R1–R3 in Fig. 17(a)] become fourfold coordinated. Noticeably, Si adatoms A1–A3 are displaced towards the triangle center considerably, which strengthens their bonds with the substrate atoms by resuming the 109.5°-tetrahedral angles. Each Si adatom has two 80°, one 83°, and three close-to-tetrahedral angles. Thus, by displacing Si adatoms not only can the perceived steric strain be avoided, but also the displaced Si adatoms serve as the "missing" links between the otherwise loosely packed In atoms. The calculation also shows that an In cluster on the UFHUC is 0.1 eV/cluster higher in energy than that on the FHUC, which also agrees with the experimental result that most In clusters occupy the FHUC of Si(1110-7 × 7) preferentially.

The calculated STM images in Fig. 17(e) and (f) are in remarkable qualitative agreement with experiment [Fig. 17(b) and (c)]. Interestingly, in the empty state image [Fig. 17(e)], the three brightest spots are from the lowest In atoms, which are 0.6 Å lower than Si A1–A3 with an average bond angle of 105° (thus sp^3-like). The three second-brightest spots are from the other In atoms, which are 0.3 Å lower than Si A1–A3 with an average bond angle of 115° (thus sp^2-like). Si adatoms A1–A3 are almost invisible, as they do not involve any dangling bond. Another striking feature in Fig. 17(c) is the disappearance of the six-In triangle spots under small *reverse* bias, whereas the three Si corner adatom spots (A4–A6) become significantly brighter. The calculation reveals that this change is not due to In diffusion but has an electronic origin. The calculated density of states reveals a 0.33 eV band gap 0.2 eV below the Fermi energy (E_F). States below the gap have mainly the Si/In bonding character. States above the gap but below E_F have mainly the dangling-bond character and are predominantly on Si A4–A6. The In dangling bond states are found to be above E_F thus can only be seen in the empty state image.

This application also demonstrates that STM combined with first-principles total energy calculations is a very powerful method to determine the atomic structure of surfaces with/without adsorbates. The atomic structures of Al and Ga nanoclusters have also been determined by this method [31, 32]. Some other metal (including alkali metals) clusterss were also fabricated this way [33].

2.2. Metal Surfaces

2.2.1. Metal Surfaces

Metal surfaces had been studied for more than two decades before STM was invented. In 1982, the Au(110)-2 × 1 surface was first imaged with STM by Binnig *et al.* [34]. This work confirmed the missing-row model proposed for this surface although atomic resolution was not achieved.

For non-reconstructed metal surfaces, the charge density corrugation amplitudes are typically on the order of 0.1 Å since STM usually probes the delocalized s- or p-type states, while the corrugations for semiconductor surfaces are often of several Å due to the presence of dangling bonds. Metal corrugations are usually 50–100 times smaller than those on the Si(111) 7 × 7 surface, and thus, it is much more difficult to obtain atomic resolution on metal surfaces than on semiconductor surfaces. With the development of STM instrumentation, more and more investigations on metal surfaces were reported. In 1987, the first atomic resolution STM image was observed on the Au(111) surface [35], which strongly impacts the STM investigation on metal surfaces. Au(111) has been the most widely used metal substrate in STM studies because the surface is inert and atomic resolution STM images can be obtained even in air.

Clean Au(111) surface reconstructs to ($23 \times \sqrt{3}$) reconstruction. The "herringbone structure" reconstruction can be easily observed by STM, as shown in Fig. 18(a). An atomically resolved image of a bending point is shown in Fig. 18(b) [36, 37]. This structure is explained by the stacking-fault-domain model, which involve stacking faults between fcc and hcp orderings induced by surface strain.

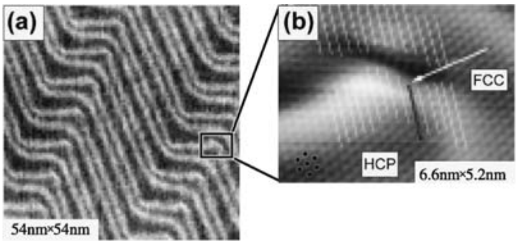

Figure 18. STM images of Au(111)-(23 × √3) surface. (a) "herringbone structure", image size: 54 nm × 54 nm. (b) atomic resolution image at the bending point (6.6 nm × 5.2 nm). (From Ref. 37)

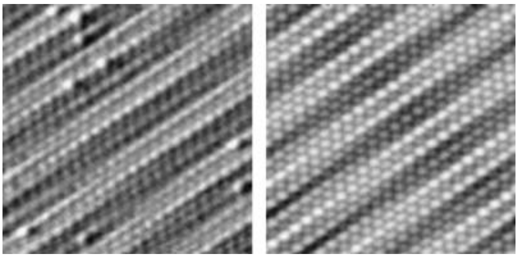

Figure 19. STM (left) and simulated (right) images of Au(001). (From Ref. 38)

For the clean reconstructed Au(001) surface, by comparing the atomic resolution STM images with simple simulations (see Fig. 19), it was found not only that the topmost atomic layer is, qualitatively, quasi-hexagonal and incommensurate, but also that it is, quantitatively, rotated by 0.1° relative to the substrate and contracted by 3.83% and 4.42% compared to a perfect (111) layer of Au, in the vertical and horizontal orientation, respectively [38].

STM has been applied to low-index surfaces of many other metals, *e.g.*, Pt, Pd, Cu, Ag, Al, *etc.* and atomic resolution has been achieved for all of them. In contrast to semiconductor surfaces, the bias voltage dependence usually is not observed on clean metal surfaces, which makes the interpretation of the STM images rather simple.

2.2.2. Adsorption on Metal Surfaces

Metal surfaces with adsorbates, especially with molecular adsorbates nowadays become increasingly important, because of their application potential in nano- and bio-science and technology [39]. Since amino acids are building blocks of proteins, adsorption of amino acids on metal surfaces, as a biological model system, has been receiving much attention [40]. Despite that in most cases each amino acid molecule can only be imaged as one protrusion, many important results about the amino acid adsorbates were obtained in a series of recent STM investigations by Zhao and coworkers, and are summarized briefly as follows.

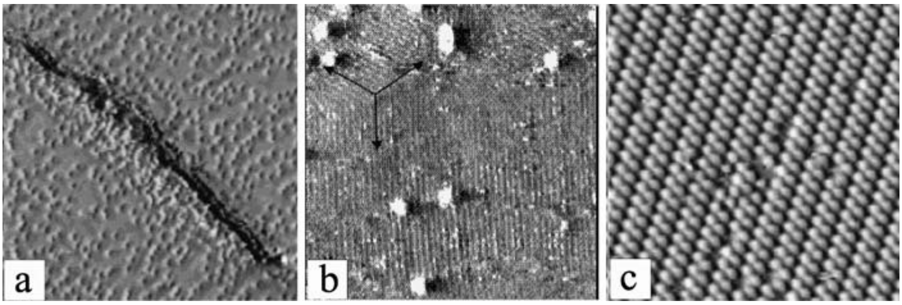

Figure 20. Three different phases of glycine adsorbed on Cu(111): (a) the 2D gas phase; (b) the chain phase; (c) the 2D solid phase. (From Ref. 41)

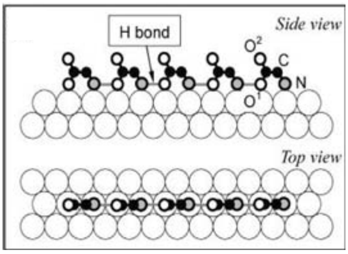

Figure 21. Schematic drawing of the chains formed by glycine molecules adsorbed on the Cu(111) surface. (From Ref. 45)

(i) Through "cook-and-look" or "anneal-and-image", it was able to determine the desorption temperature and, in turn, the binding energy of the adsorbates, and then to find if the adsorbates are chemisorbed or physisorbed on the surface. For instance, glycine was found to be chemisorbed on Cu(001) [41], while to be physisorbed on Au(110) [42].

(ii) Depending on the coverage and deposition rate, amino acid adsorbates on Cu and Au surfaces may form three different phases, i.e., the 2D gas phase, the chain phase, and the 2D solid phase (Fig. 20). Some amino acids are able to form all the three phases on Cu(001), while some others can form only one or two of the three. In the 2D gas phase the molecules are "standing" on the surface and can diffuse frequently on the surface at room temperature. The activation energy barrier was determined to be around 0.85 eV [41]. In the 2D solid phase the molecules are connected by H bonds to form different ordered structures, depending on their side chain structure [43, 44]. However, in the chain phase, different amino acids (*i.e.*, with different side chains) adsorbed on different substrates are connected by H bonds to form, surprisingly, always the same kind of 1D chains (see Fig. 21 and Ref. 45).

(iii) Moreover, amino acid adsorbates were found to be able to modify the substrate morphology significantly. For instance, adsorbates of the smallest amino acid, *i.e.*,

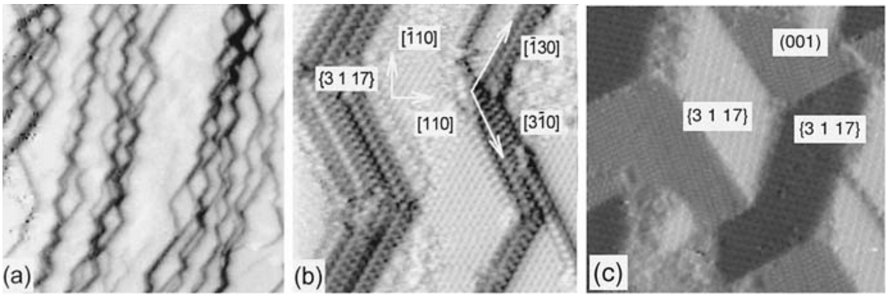

Figure 22. (a, b) Adsorption of glycine, which is not chiral, on Cu(001) makes surface steps faceting to all eight possible <310> directions and then bunching into all eight possible {3 1 17} facets [Zhao *et al.*, Surface Science 424, L347 (1999)]. (c) Adsorption of L-lysine on Cu(001) surface, in contrast, makes steps bunching only into the four {3 1 17} facets that have the same chirality. [From Zhao et al., Chinese Physics 10 (supplement), (S84 2001).]

glycine, can make all steps on the Cu(001) surface faceted (or reoriented) into eight equivalent <310> directions and then bunching into all eight equivalent {3 1 17} facets.

However, adsorption of homochiral amino acids, such as L-lysine, on the same Cu(001) surface makes the steps bunching into only the four of all eight {3 1 17} facets that have the same chirality, which is determined by the chirality of the molecules [46]. The possibility of using homochiral adsorbates to fabricate homochiral facets on a substrate is of current interest because of its potential application in chiral separations.

2.3. Insulator Surfaces

In principle, insulators cannot be studied with STM since tunneling current cannot be established between a conducting tip and an insulator. However, under some special conditions, STM observation can be performed on insulating materials. For example, BN thin film on Rh(111) surface have been investigated with STM [47]. The STM images of 2ML BN grown on Rh(111) surface by high-temperature decomposition of borazine are shown in Fig. 23. Ordered BN nanomesh is observed in the large scale image [Fig. 23(a)]. In high resolution image [Fig. 23(b)], it is clearly seen that the nanomesh consists of two layers of BN and they are offset in such a way as to expose a minimum metal surface area. NaCl(111), ZnO(0001) and TiO_2 etc. have also been reported to be studied with STM [48–50].

Recently, K. Bobrov *et al.* demonstrated that STM can be used in an unconventional resonant electron injection mode to image insulating diamond surfaces and to probe their electronic properties at the atomic scale [51]. The hydrogen-free diamond surface is insulating, no tunneling current could be obtained at any bias voltages between −6 V and +4 V. The STM tip crashed on the surface if trying to establish a tunnel current in the range 0.05–1 nA. However, at very high sample bias (+5.9 V), *i.e*, above the diamond work function (5.3 V), atomic resolution STM image can be obtained on the diamond surface as shown in Fig. 24. In Fig. 24(a), terraces rotated by 90° are clearly visible. The periodic structure of bright and dark lines is observed on every

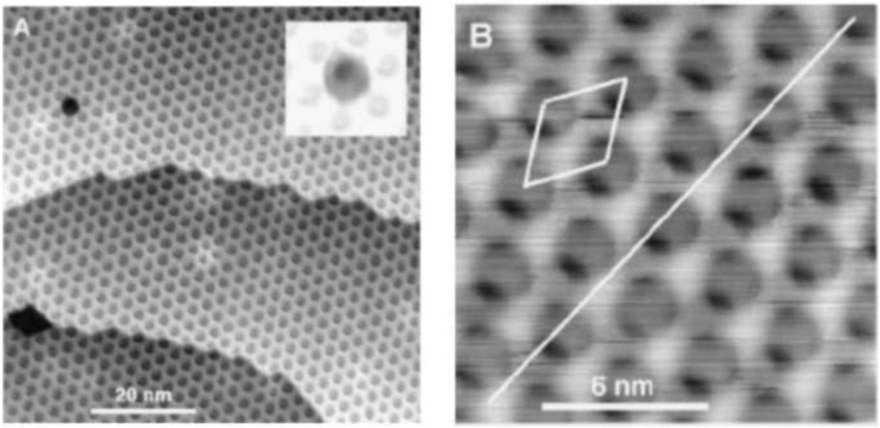

Figure 23. Constant-current STM images of the boron nitride nanomesh formed on a Rh(111) surface. (a) Large-area image taken with a bias voltage of $V_b = -1.0$ V and a tunneling current of $I_t = 2.5$ nA. The black features are defects in the mesh, one of which is shown with different contrast in the inset. (b) High-resolution image (–2.0 V and 1.0 nA) clearly showing the presence of two layers of mesh that are offset such as to cover most of the Rh(111) surface. The mesh unit cell is indicated (From Ref. 47).

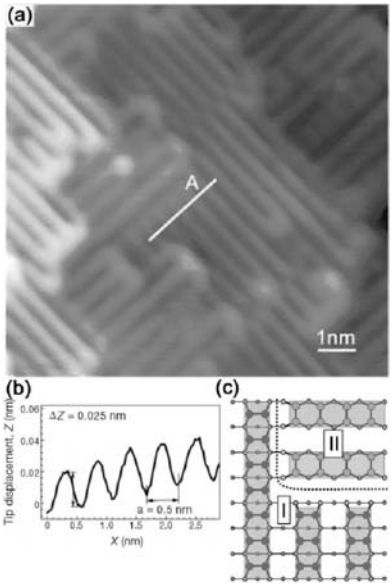

Figure 24. Clean diamond C(100)-(2 × 1) surface. (a) The STM topography (10 nm × 10 nm) of the clean diamond surface recorded in the near-field emission regime (Ub = 5.9 V, I = 1.1 nA). (b) Height variation of the STM tip along the line A. (c) Topview of a monoatomic step on the two-domain (2 × 1) reconstructed surface. The circles represent the carbon atoms belonging to the top four surface layers; the biggest circles represent the carbon-carbon dimers. The domains labelled as I and II represent the upper and lower terrace, respectively. The dimer rows are highlighted by shading. The dashed line shows schematically the boundary between the domains. (From Ref. 51)

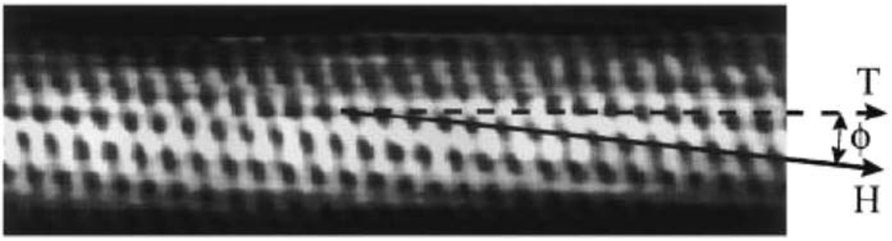

Figure 25. Atomically resolved STM image of individual single-walled carbon nanotubes. The lattice on the surface of the cylinders allows a clear identification of the tube chirality. Dashed arrows represent the tube axis T and the solid arrows indicate the direction of nearest-neighbour hexagon rows H. From the image, it can be determined that the tube has a chiral angle $\varphi = 7^\circ$ and a diameter $d = 1.3$ nm. (From Ref. 53)

terrace. The periodicity of ~0.5 nm, as measured from the scan profile shown in Fig. 24(b), agrees well with the distance (0.504 nm) between the C–C dimer rows of the (2 × 1) reconstructed diamond surface. This work suggests that STM can be operated in the near-field emission regime and this method can be applied to investigate other insulating materials.

2.4. Nanotubes and Nanowires

Carbon nanotubes have attracted much attention since their discovery in 1991 due to their peculiar properties [52]. STM has been widely used to study the structure and electronic properties of carbon nanotubes [53–55]. An atomically resolved STM image of individual single-walled carbon nanotubes is shown in Fig. 25, from which, the structure (chiral angel and diameter) can be easily determined. Combined with scanning tunneling spectroscopy (STS, which will be introduced in the next section), their local electronic properties can also be related to the local structures [53].

Shown in Fig. 26 is an STM image of an oxide-removed Si nanowire, another kind of interesting nanowires [56]. The study also showed that the electronic energy gaps of Si nanowires increase with decreasing Si nanowire diameter from 1.1 eV for 7 nanometers to 3.5 eV for 1.3 nanometers, in agreement with previous theoretical predictions.

In these studies, highly ordered pyrolytic graphite (HOPG), Au(111) or Au film are often used as substrates, whereas nanotubes and nanowires are usually deposited on the surface from dilute solutions. The outmost structure of the nanotubes and nanowires can be determined from atomically resolved STM images. In addition, STS is often used to probe their electronic properties and the relationship between electronic properties and structures. Such information is very difficult to obtain with other techniques.

2.5. Surface and Subsurface Dynamic Processes

So far, it has been shown that the atomic structure of many different surfaces can be studied or even determined on the basis of high-resolution STM images. With atomic

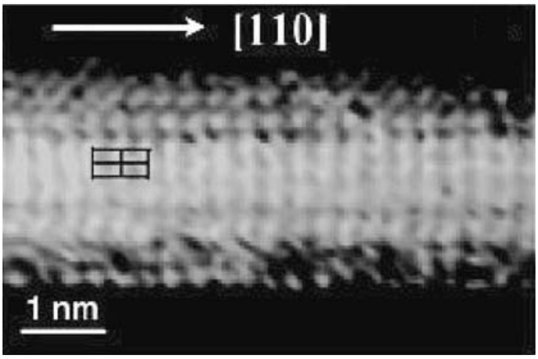

Figure 26. STM image of a Si nanowire with a Si(001) facet. The wire's axis is along the [110] direction. (From Ref. 56)

resolution STM images, it is also possible to study surface or even subsurface atomic dynamic processes.

2.5.1. Surface Diffusion

Although it is possible to study surface diffusion by checking the position of individual atoms, to find out, among hundreds or more atoms, the few that diffused from one image to another is nevertheless tedious. However, difference images obtained from a set of sequential images can make the job much easier (see Fig. 27). It was thus found that on the Ge(111) surface individual adatoms neighboring to some defects are able to diffuse even at room temperature [57]. Moreover, it was also found that, if the domains are not very large, adatoms forming a string or closed loop lying along domain walls may diffuse one after another (see Fig. 27). In addition, the mean lifetime of the diffusing adatoms can also be determined and from which the diffusion energy barrier of the adatoms was deduced to be 0.83 ± 0.02 eV, in good agreement with its theoretical value.

2.5.2. Subsurface Migration

Despite that STM is a very surface sensitive technique, from the difference images of a set of sequential images of the Ge(113) surface it was also able to find that the subsurface self-interstitial atoms are migrating frequently even at room temperature, making the local surface structure changing back and forth between (3×2) and (3×1) Fig. 28(a) and (b). Interestingly, migration of a subsurface self-interstitial atom into or out of a place results in a quite large and complicated feature around that place in the difference image, as shown in Fig. 28(c). However, considering that each subsurface atom is bound to several surface atoms this is actually quite reasonable. Furthermore, the lifetime of the self-interstitials was determined to be 400 s at room temperature, and their migration energy barrier was deduced accordingly to be 0.93 ± 0.02 eV [58].

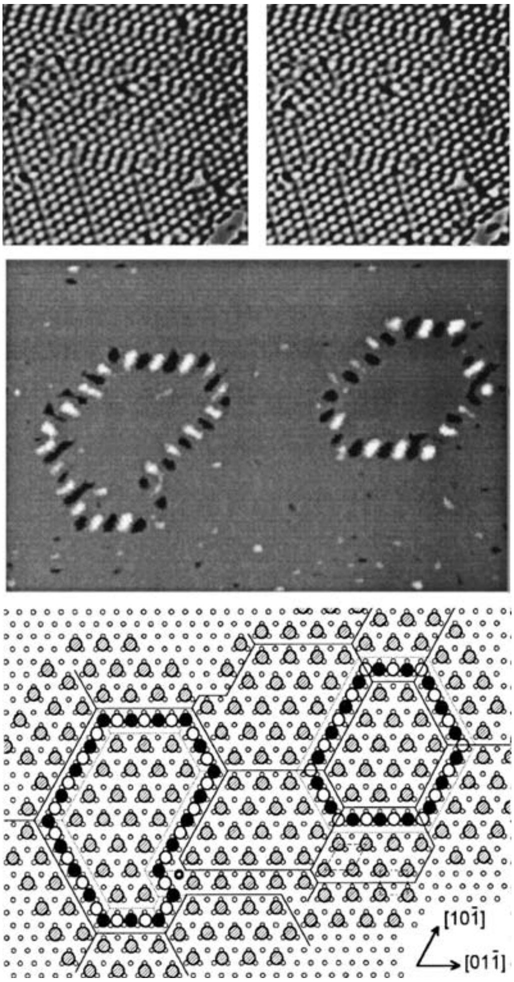

Figure 27. (a) STM image obtained from a Ge(111) surface (b) STM image obtained from the same place as in (a) but 6 minutes later. (c) Portion of the difference image obtained by subtracting (b) from (a), showing shifts of tens of the adatoms forming two closed loops. (d) Schematic drawing of (c), showing the details relevant to the adatom shifts. (From Ref. 57)

2.5.3. Movement of Subsurface Dislocations

Another type of subsurface defects, subsurface dislocations, can be found with STM as small regular bumps on many annealed metal surfaces, although argon ion bombardment or STM tip touching can induce more of them. In the case of Au(001) where, as mentioned above, the topmost atomic layer is incommensurate with the substrate and thus Moiré fringes appears on the surface. It was shown that such Moiré fringes can be used as "magnifier" to study the details of such subsurface dislocations, including

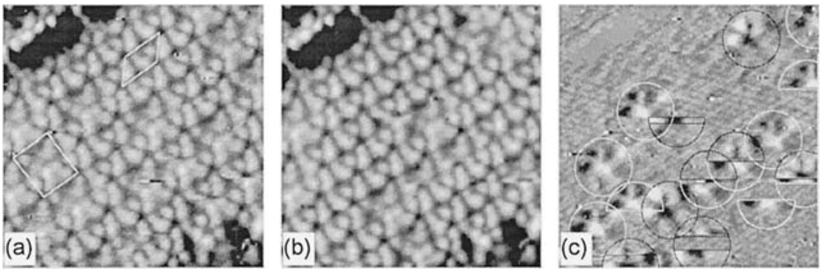

Figure 28. (a, b) Two consecutive STM images (70 × 70 Å^2) obtained from a Ge(113) facet, with a (3 × 1) and (3 × 2) unit cell outlined in (a). (c) The differential image obtained by subtracting (b) from (a). The circled areas are those where a subsurface self-interstitial atom migrated in or out between or during imagings. (From Ref. 58)

their extremely slow movement and the weak strain fields that push them to move. Specifically, on the basis of STM and simulated images, a precision of better than 0.1 Å was achieved in determination of the lateral strain fields and a dislocation speed lower than 1 Å/min was measured [38]. As Moiré fringes exist in many surfaces and adsorbate systems, the method is expected to have wide applications.

3. SCANNING TUNNELING SPECTROSCOPIES

As mentioned above, bias-dependence of STM images is often observed, particularly for semiconductor surfaces, which makes it difficult to explain the STM images. However, very useful spectroscopic information can be extracted from the bias-dependence of tunneling current. In fact, tunneling spectroscopy had been used with fixed tunneling junctions before STM was invented. More important information can be obtained by measuring tunneling spectroscopy with an STM. The scanning ability of STM makes it possible to probe local spectroscopic signals with atomic spatial resolution. By changing the tip-sample distance, the potential barrier can also be investigated with STM.

3.1. Scanning Tunneling Spectroscopy (STS)

From Eq. 10, tunneling current at a finite bias voltage V can be expressed as:

$$I \propto \int_0^{eV} \rho_S(E_f - eV + \varepsilon)\rho_T(E_f + \varepsilon)d\varepsilon, \tag{12}$$

where, ρ_S and ρ_T are the DOS of sample and tip respectively. If ρ_T is constant, then:

$$\frac{dI}{dV} \propto \rho_S(E_f - eV + \varepsilon), \tag{13}$$

i.e., the structure in dI/dV as a function of V represents the structure in the DOS of sample, which is called as scanning tunneling spectroscopy (STS).

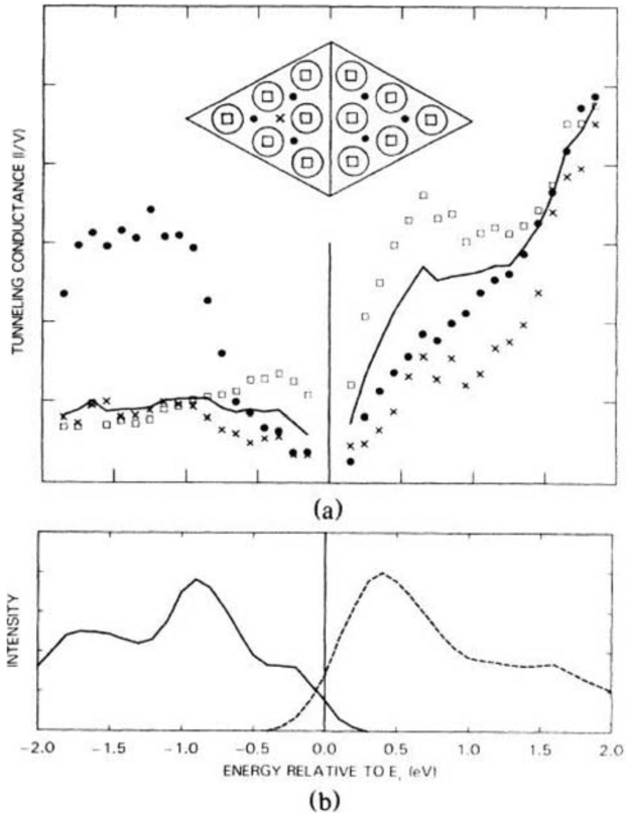

Figure 29. (a) Constant-distance $I/V \sim V$ spectra for the Si(111)-7 × 7 surface averaged over one unit cell (solid line) and at selected locations in the unit cell (other symbols). (b) Spectra obtained with UPS (solid line) and IPS (dashed line). (From Ref. 59)

The first spatial resolved tunneling spectroscopy was demonstrated by Hamers *et al.* on Si(111) 7 × 7 surface [59]. The site-selected conductance curves ($I/V \sim V$) within a Si(111)-7 × 7 unit cell are shown in Fig. 29. The physical origin and the nature of the surface states of Si(111)-7 × 7 surface, including the states due to dangling bonds on twelve adatoms, the states localized on rest atoms, the states due to Si-Si backbonds, and the states localized in the deep corner hole were directly identified. The $I/V \sim V$ spectra averaged over one unit cell is comparable with the results of ultraviolet photoemission spectroscopy (UPS) and inverse photoemission spectroscopy (IPS). Better agreement between the spectrum averaged over an area encompassing many unit cells and the data from UPS and IPS were achieved later [60]. These studies showed that the electronic structure of the tip is relatively unimportant in STS measurements.

Current imaging tunneling spectroscopy (CITS) was also proposed, which allows real-space imaging of surface electronic states. By measuring constant separation I–V

curves at each point during scanning, current images at sample voltages within a range can be obtained simultaneously with STM topographic image. The resulting real-space current images directly reflect the spatial distribution of the surface states without interference from geometric structure contributions [59]. The atomic resolved CITS images on Si(111)-7×7 surface are shown in Fig. 30, from which the atomic origins of the various electronic states can be easily determined. The electronic states near -0.35 eV are from the 12 adatoms, the states near -0.8 eV arise from the 6 rest atoms, whereas the states near -1.7 eV are from backbond states.

The capability of identifying surface states in real-space with atomic resolution greatly extends the utility of STM as a spectroscopic tool. STM combined with STS has been widely used to study the structure, electronic properties and their relationship of various materials.

3.2. Inelastic Tunneling Spectroscopy

By now, we only considered the elastic electron tunneling process, in which the electrons keep conservation of energy during tunneling. In fact, inelastic tunneling can also occur if the tunneling electrons couple to some excitation modes in the tunneling junction. In 1966 it was discovered that inelastic electron tunneling spectroscopy (IETS) can be obtained from molecules adsorbed at the buried metal-oxide interface of a metal-oxide-metal tunneling junction [61]. With the development of STM, it was apparent that IETS might be performed on a single molecule in the junction of a STM (STM-IETS) [62]. The metal-oxide-metal tunnel junction is replaced by the STM tunnel junction: a sharp metal tip, a vacuum gap of several angstroms, and a surface with the adsorbed molecules. The combination of atomic resolution and IETS allows the creation of atomic-scale spatial images of the inelastic tunneling channel for each excitation mode, in a manner similar to that used to map out the electronic density of states with the STM [59]. Unfortunately, the conductance changes caused by inelastic tunneling are less than 10% for the STM. Therefore, the extreme mechanical stability is necessary to obtain reasonable IETS with the STM. In addition, low temperature is required to keep thermal line-width broadening small compared with the inelastic exciting energy.

Single-molecule vibrational spectroscopy was first obtained with STM-IETS by Stipe *et al.* in 1998 [62]. To measure the IETS, a small ac modulation was added to the dc sample bias voltage, the tunneling current was fed into a lock-in amplifier to determine the first and second harmonics of the modulation frequency which are proportional to dI/dV and d^2I/dV^2, respectively. These signals were recorded as the sample bias voltage was swept from 0 to 500 mV. As shown in Fig. 31, obvious difference was found in the STM-IETS for C_2H_2 and C_2D_2 although they could not be identified in the atomic resolved STM topographic image. The C-H stretch at 358 mV for C_2H_2 was observed to shift to 266 mV for C_2D_2 (Fig. 31). These values are in close agreement with the results obtained by EELS.

By doing IETS, it is possible to identify molecules with the STM, which permits to implement chemically sensitive microscopy. Vibrational imaging of the adsorbed

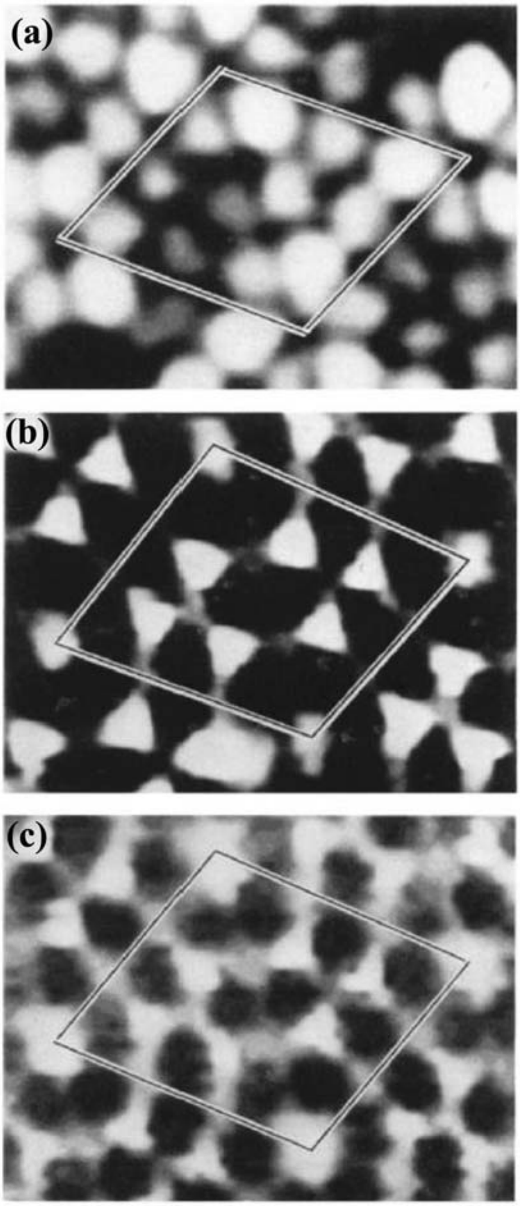

Figure 30. CITS images of occupied Si(111)-7 × 7 surface states. (a) adatom states at −0.35 V, (b) dangling-bond state from rest atoms at −0.8 V, (c) backbond state at −1.7 V. (From Ref. 59)

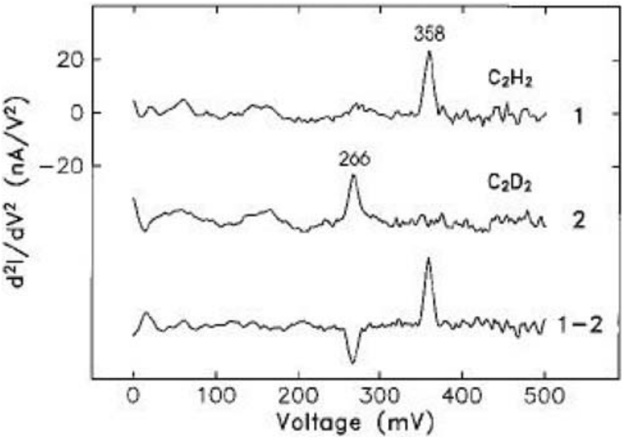

Figure 31. Background difference d^2I/dV^2 spectra for C_2H_2 (1) and C_2D_2 (2), taken with the same STM tip, show peaks at 358 mV and 266 mV, respectively. The difference spectrum (1–2) yields a more complete background subtraction. (From Ref. 62)

molecule was obtained by recording dI/dV and d^2I/dV^2 at each data point with the feedback off and the bias modulation on while scanning the tip in constant-current mode. This procedure results in three images of the same area. In a constant-current image, no contrast was observed for both acetylene isotopes [Fig. 32(A)]. When the dc bias voltage was fixed at 358 mV, only one of the two molecules was revealed in the image constructed from the d^2I/dV^2 signal [Fig. 32(B)]. By changing the dc bias voltage to 266 mV, the other molecule was imaged [Fig. 32(C)]. Two small identical depressions observed at 311 mV [Fig. 32(D)] were attributed to the change in the electronic density of states on the sites of the two molecules [62].

STM-IETS extends the vibrational spectroscopy to the single-molecule limit and provides the STM with chemical sensitivity. Combination of the high spatial resolution of STM and IETS permits to correlate variations in molecular spectra with changes in the local environment on an atomic scale [63].

3.3. Local Work Function Measurement

The general definition of the work function, i.e., the minimum energy needed to remove an electron from a metal to infinity, is clear but cannot be used to measure the local work function. Wandelt, considering that surface dipole potentials reach their saturation value already within ∼2 Å from the surface, defined the local work function (LWF) as the local surface potential measured from the Fermi level E_F, which allows us to measure LWF variations induced by surface dipole patches [64, 65]. In this definition, the LWF probe can be put close to the surface compared to the dimensions of the surface patch under study. Obviously, the closer the probe is to the surface the smaller the surface patch of interest can be, provided that presence of the probe has no

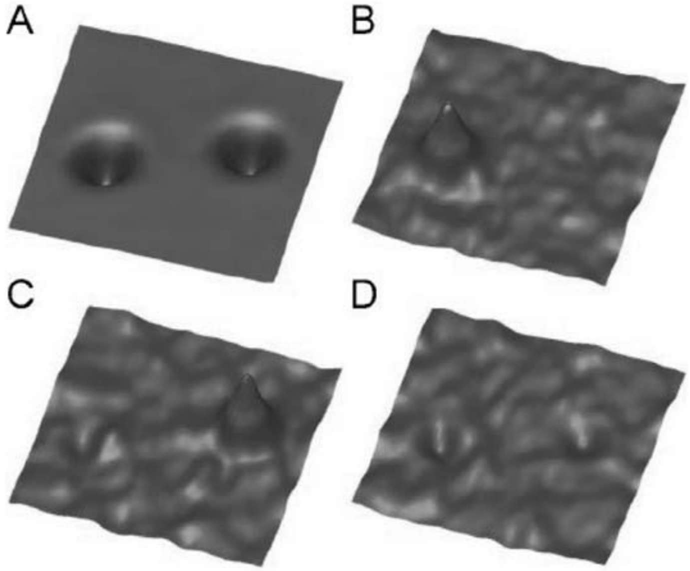

Figure 32. Spectroscopic spatial imaging of the inelastic channels for C_2H_2 and C_2D_2. (A) Regular (constant current) STM image of a C_2H_2 molecule (left) and a C_2D_2 molecule (right). The imaged area is 48 Å by 48 Å. d^2I/dV^2 images of the same area recorded at (B) 358 mV, (C) 266 mV, and (D) 311 mV. All images were scanned at 1 nA dc tunneling current. (From Ref. 62)

influence on the local surface potential, and hence this LWF definition is suitable for studying LWF variation with STM.

Work function is important in STM because it determines the height of the tunneling barrier. The tunneling current I depends exponentially on the tip-sample distance s:

$$I \propto \exp(-2\kappa s), \text{with}\, \kappa = \hbar^{-1}(2m\phi)^{1/2}, \tag{14}$$

where ϕ is the effective local potential barrier height. From the above formula, we have

$$\phi_A[eV] = \frac{\hbar^2}{8m}^{-1}\left(\frac{d\ln I}{ds}\right)^2 \approx 0.95\left(\frac{d\ln I}{ds\,[\text{Å}]}\right)^2. \tag{15}$$

Binnig and Rohrer have shown that, at least in the image force range, the s dependence enters ϕ_A in second order only, or ϕ_A is nearly independent of the tip-sample separation. Moreover, it has also been pointed out that for homogeneous surfaces ϕ_A is work function [66], while for patchy surfaces, ϕ_A is equal to the LWF [65].

In an experiment, the height of the tunneling barrier or work function can be obtained by measuring the response of the tunneling current when changing the gap

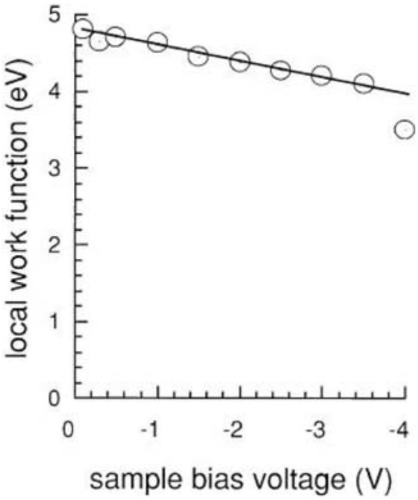

Figure 33. Measured work function dependence on sample bias voltage for Cu(111) surface. (From Ref. 69)

distance. Actually, at the beginning of the STM invention by Binnig and Rohrer, they already pointed out the possibility of measuring the work function and taking its image [67]. Jia *et al.* have measured the LWF on metal surfaces quantitatively [65, 68, 69]. In their experiments, the modulation frequency was set at 2.0 kHz, higher than a cut-off frequency of the feedback loop of the STM system they used (~1 kHz) but lower than the response frequency of the current amplifier of the STM. The frequency dependence of the work function on the Cu(111) substrate showed that the modulation frequency (2.0 kHz) is in a plateau range. The amount of modulation in the gap distance is 0.23 Å, much smaller than the gap distance, 5.5–6.0 Å.

The LWF dependence on bias voltage measured using a Cu(111) surface is shown in Fig. 33. From these measurements, it turns out that the work function drops slowly with a ratio of ~0.2 eV/V as the bias voltage increases gradually up to −3.5 V. Variation of work function with a bias voltage is quite reasonable because applying a bias voltage lowers the barrier height in the STM gap. It is qualitatively consistent with the results of previous experimental and one-dimensional numerical simulation. At a low bias voltage limit, it reaches around 4.8 eV, close to an average value of work function of Cu(111) and W(111), which is used for the probing tip. Image potential does not seem to contribute so much to the work function [69].

By measuring LWF at each point during scanning, a LWF image can be obtained simultaneously with a STM image. Figure 34(b) is the LWF image taken simultaneously with the STM image in Fig. 34(a). From the STM image alone it is rather difficult to distinguish the Au-covered areas from those uncovered, although from the former one can vaguely see the quasi-periodic triangular features. As the Au terraces have a

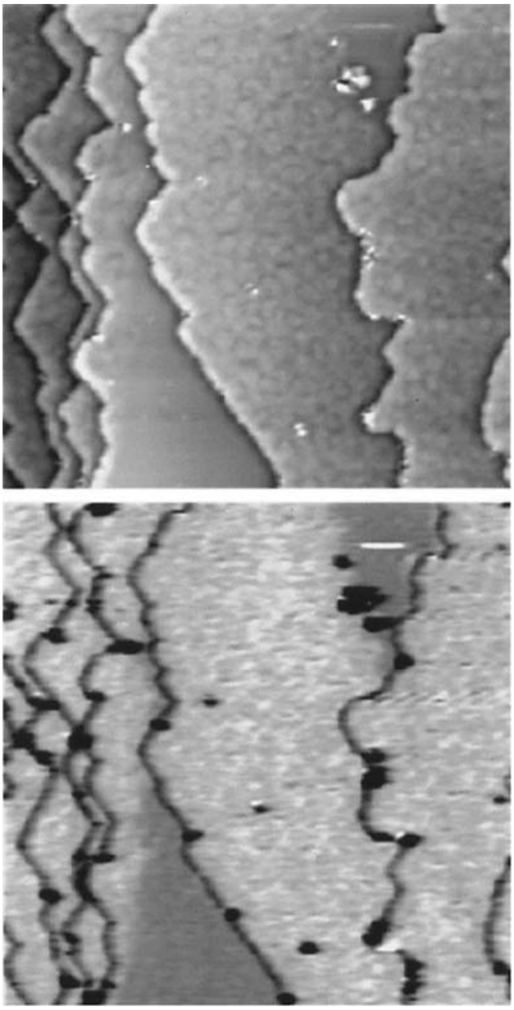

Figure 34. (a) STM images of a Au/Cu(111) surface (580 Å × 580 Å). (b) Simultaneously obtained work function image. The mean value of the work function on the Au overlayer (bright area) is 7% higher than that on the Cu(111) substrate (dark area). The dark lines correspond to a low work function zone at step edges. (From Ref. 68)

higher WF than that of the Cu terraces we identify the brighter areas in the WF image as covered by a Au layer, while the darker areas as being nude.

Similar measurements have been carried out using a Pd/Cu(111) surface [68]. An STM image obtained from the surface is given in Fig. 35(a), and the corresponding work function image [Fig. 35(b)] shows that work function measured on Pd overlayers is larger than that of the Cu substrate. The conclusion of the statistical analysis is that the first Pd layer has a larger work function than Cu(111) by 19 ± 5%. The dark contrast

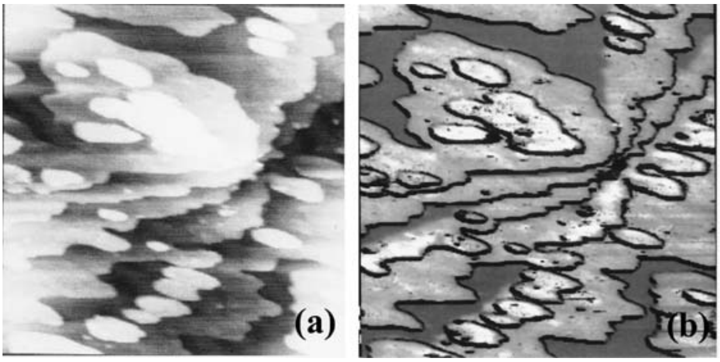

Figure 35. (a) STM and (b) work function images obtained on a Pd/Cu(111) surface. The applied sample bias voltage is −2.0 V, and the tunneling current is 0.1 nA. The size of the observed area is ~570 Å × 570 Å. The coverage of Pd is ~1.0 ML. It shows that the Pd layer has a higher work function than the Cu substrate and that the second Pd layer has a higher work function than the first Pd layer. (From Ref. 68)

along step edges is observed in the work function images taken on the Pd/Cu(111) surface as well.

Different from the results on Au/Cu(111) surface, the second layer of Pd shows a higher work function than the first layer of Pd. In this image, islands of the first Pd layer are observed on a wide terrace of the Cu substrate, and several small islands of the second Pd layer are observed on them. In the corresponding work function image [Fig. 35(b)], islands of the second layer look brighter than those of the first layer, indicating a higher work function on the second Pd layer than on the first Pd layer. According to their statistical analysis, the work function of the second layer Pd is larger than the first layer Pd by 6 ± 5%.

Quantitative analysis shows that the work function measured for the first Pd layer is already larger than that of bulk Pd(111), and it further increases with increasing thickness of Pd. This kind of overshooting of LWF measured for Pd film could be the quantum size effect on the work function since film thickness of the overlayers is smaller than the Fermi wavelength of the metals [68].

In the LWF images obtained from both the Au/Cu(111) surface [Fig. 34(b)] and Pd/Cu(111) surface [Fig. 35(b)] dark valleys along steps can be observed, indicating that the LWF at steps is much lower than that on terraces. This agrees with the fact that the work function decreases with increasing step density [70]. To show more details, a line scan crossing a step that separates two Au terraces is shown with a solid line in Fig. 36(a). According to the statistic based on more than 100 WF images like Fig. 34(b), the mean full width at half maximum and depth of the LWF valley for Au-Au monatomic steps are 6.5 ± 1 Å and 0.9 ± 0.3 eV, respectively, while for Cu-Cu monatomic steps are 10 ± 1 Å and 1.9 ± 0.3 eV, respectively.

Dipoles induced by Smoluchowski smoothing effect [71] at steps are very likely responsible for the formation of such LWF valleys. A simple simulation has thus been

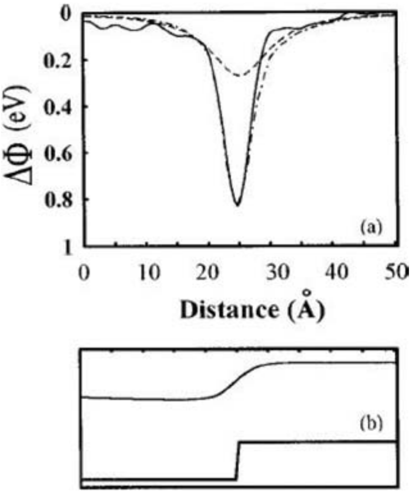

Figure 36. (a) Comparison of the experimental local work-function profile crossing an Au-Au monatomic step (solid line) with its simulated counterpart (dashed-dotted line). The reduction induced by the step dipoles alone is also shown (dashed line). (b) STM line scan (top) obtained simultaneously with the solid line in (a), and the schematic step profile showing the location of the step. (From Ref. 65)

made accordingly, where an infinite row of equal dipoles is used to simulate a step. If a right-hand coordinate system is set such that the axis of the dipole row lays long the y-coordinate axis with the positive end of the dipoles pointing to the outside of the surface, i.e., the $+z$ direction, then the local surface potential at a point (x, z) induced by the dipole row is given by:

$$\phi_D(x, z) = \left(\frac{Q}{4\pi\varepsilon_0}\right)\ln\frac{(z+l/2)^2+x^2}{(z-l/2)^2+x^2}, \tag{16}$$

where Q is the linear density of charge, l is the distance between the positive and negative charges. Let d be the spacing of the step atoms; then the induced dipole moment can be calculated as $\mu = Qdl$ per step atom. Since it is the constant-current rather than the constant height mode that was used in the experiment, to simulate the LWF line scan shown in Fig. 36(a) with Eq. 16, what they have to calculate is not $\phi_D(x, z_0)$ but $\phi_D[x, z(x)]$, where $z(x)$ is the real STM line scan [the top curve in Fig. 36(b)], along which the LWF is probed. Note that the line scan is quite different from the schematic step profile, which is expected to be more like the profile of the real step. The reason for this is twofold: Smoluchowski smoothing [71] as mentioned above, and obviously, convolution with the tip. However, as pointed out by Binnig and Rohrer [72], the step topography has one more effect on the measured values of LWF because what is measured, as mentioned above, is the response $d(\ln I)$ to the modulation of the gap distance ds, which ought to be in the normal direction of the surface. If at a point the normal of the surface is not in the z direction but tilted away by an angle θ

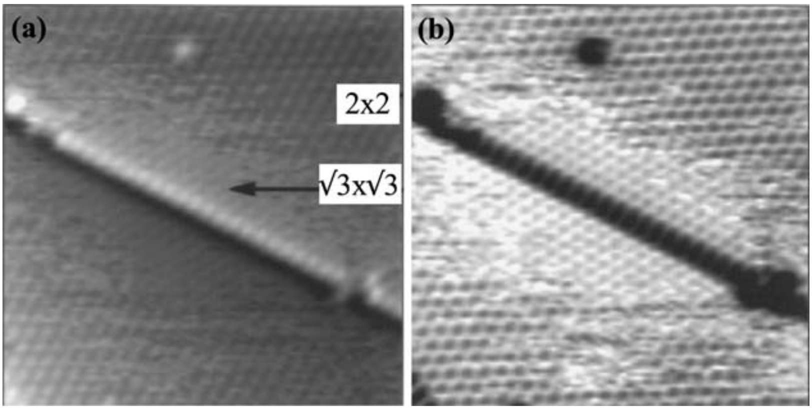

Figure 37. Atomic resolved STM (a) and work function (b) images on S/Pt (111) surface. The scanning area is 120 Å × 120 Å, containing both 2 × 2 and $\sqrt{3} \times \sqrt{3}$ reconstruction. It is demonstrated that the $\sqrt{3} \times \sqrt{3}$ structure has larger work function than 2 × 2 structure. (From Ref. 73)

then the real *ds* is reduced by a factor of $\cos\theta$ even if the modulation of the tip height *dz* is constant. As a result, the measured local work function of that point is reduced by a factor of $\cos^2\theta$. So, after taking this into account in the simulation, the LWF variation around a step is then calculated as

$$\Delta\phi(x) = \phi_{AT} - [\phi_{AT} - \phi_D(x, z)]\cos^2\theta, \tag{17}$$

where ϕ_{AT} is the measured LWF of the terraces that are separated by the step, and $\phi_D(x, z)$ is the potential of the dipole row along the step and hence is given by Eq. 16. In the calculation the value of θ at each point was determined from the real STM line scan and the distance between the positive and negative charges l was set to be the step height (l has almost no effect on the final results). By optimizing the gap distance and the linear density of dipole moment, a good agreement between the calculated and experimental curves has been achieved. The calculated $\Delta\phi(x)$ and $\phi_D(x, z)$ are shown in Fig. 36(a) as the dotted-dashed and dashed lines, respectively, along with the experimental curve (solid line) for comparison. The tip height is 4.9 Å, and the dipole moment is $\mu = 0.16 \pm 0.05$ D/step atom, in agreement with the value of 0.2–0.27 D/step atom derived by Besoke *et al.* from a stepped Au(111) surface [70]. A similar simulation has also been carried out for Cu-Cu monatomic steps, and the result is $\mu = 0.5 \pm 0.15$ D/step atom, which is about twice as large as that of Au-Au steps [65].

Atomic resolution can also be achieved with LWF measurement. As shown in Fig. 37, atomic resolved STM and LWF images were obtained on S/Pt(111) surface. At this coverage, 2 × 2 and $\sqrt{3} \times \sqrt{3}$ reconstructions coexist on the surface [Fig. 37(a)], the LWF image [Fig. 37(b)] shows that the $\sqrt{3} \times \sqrt{3}$ structure has a larger work function than 2 × 2 structure [73].

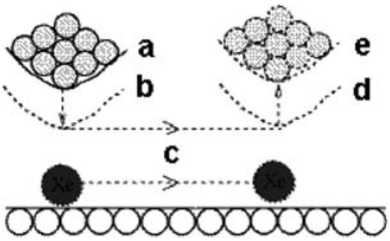

Figure 38. A schematic illustration of the process for sliding an atom across a surface. The atom is located and the tip is placed directly over it (a). The tip is lowered to position (b), where the tip-atom attractive force is sufficient to keep the atom located beneath the tip when the tip is subsequently moved across the surface (c) to the desired destination (d). Finally, the tip is withdrawn to a position (e) where the tip-atom interaction is negligible, leaving the atom bound to the surface at a new location. (From Ref. 74)

It has been shown that STM is indeed a powerful technique for measurement of LWF, and that measuring LWF with STM is very useful for elemental identification on metal surfaces. This technique provides unique information on how the atomic structure of a surfaces is related to the work function and thus is very useful for elucidating processes on solid surfaces.

4. STM-BASED ATOMIC MANIPULATION

As discussed above, STM is very powerful in studying atomic structure and electronic properties of various surfaces. In these studies, the tip-sample interaction is usually kept as small as possible so that the investigations are non-destructive. However, if one adjusts the parameters to increase the tip-sample interaction in a controlled way, STM can also be used to fabricate nano-structures down to the atomic level. Various nano-structures can be constructed by different methods, including manipulation of single atoms [74], scratching [75], oxidation [76], tip-induced chemical reactions [77–78], heating [79] and *etc.* [4]. Below, we will introduce some of them.

4.1. Manipulation of Single Atoms

Eigler and colleagues at IBM succeeded in writing "IBM" with xenon atoms in 1990 and pioneered the new field of manipulation of single atoms [74]. Toggling a single atom and pulling/pushing it on a surface were first demonstrated on the Xe adsorbed Ni(110) surface using a low-temperature UHV STM. The process to move an adsorbed Xe atom is shown in Fig. 38. The STM scanning is first stopped and the tip is placed directly above the atom (a). Then lower the tip toward the atom to increase the tip-atom interaction (b); this is achieved by changing tunneling current to a higher value (typically ~30 nA). This step is critical, the tip-atom interaction has to be strong enough to allow the atom to overcome the energy barrier to slide to neighboring place on the substrate. On the other hand, the tip-atom interaction has to be smaller than the interaction between atom and substrate so that the atom cannot be transfer from

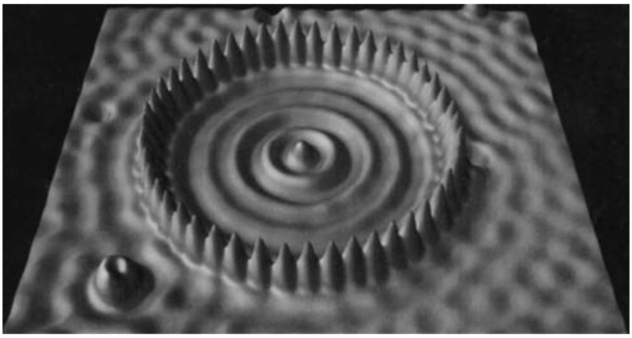

Figure 39. "Quantum corral" built with 48 Fe atoms on Cu(111) surface. (From Ref. 80)

substrate to tip. The tip (dragging the atom together) is then moved under closed-loop conditions to the desired destination slowly (c) and stops there (d). Finally, the tip is withdrawn by reducing the tunneling current to the value used for imaging (~1 nA) and leaving the atom at the destination.

By repeating this procedure to position other adsorbed atoms, structures of ones own design can be fabricated atom by atom. Using this method, "quantum corrals" was built with 48 Fe atoms on Cu(111) surface [80]. As shown in Fig. 39, the interference effects of electron waves can be clearly observed in the corral. From the dependence of periodicity of the wave on bias voltage, they could determine the effective mass of electrons in Cu(111) surface states to be about 0.37 m_e(m_e, the mass of a free electron), which is in good agreement with the value obtained by other techniques [80].

Recent, the "quantum mirage" effect was demonstrated using an elliptical corral built with Co atoms on Cu(111) surface [81]. Conventional image projection relies on classical wave mechanics and the use of natural or engineered structures such as lenses or resonant cavities. This work demonstrates that the electronic structure surrounding a magnetic Co atom can be projected to a remote location on the Cu(111) surface; electron partial waves scattered from the real Co atoms are coherently refocused to form a spectral image or "quantum mirage". The focusing device is an elliptical quantum corral, assembled on the Cu surface. The corral acts as a quantum mechanical resonator, while the two-dimensional Cu surface state electrons form the projection medium. When placed on the surface, Co atoms display a distinctive spectroscopic signature, known as the many-particle Kondo resonance, which arises from their magnetic moment. Fig. 40 shows that when a magnetic cobalt atom is placed at a focus point of elliptical corrals (a, b), some of its properties also appear at the other focus (c, d), where no atoms exists. When the interior Co atom is moved off focus, the mirage vanishes. Over 20 elliptical resonators of varying size and eccentricity were made to search for the formation of a quantum mirage. It was found that as *a* (the semimajor axis length) is increased monotonically while *e* (eccentricity) is fixed, the mirage

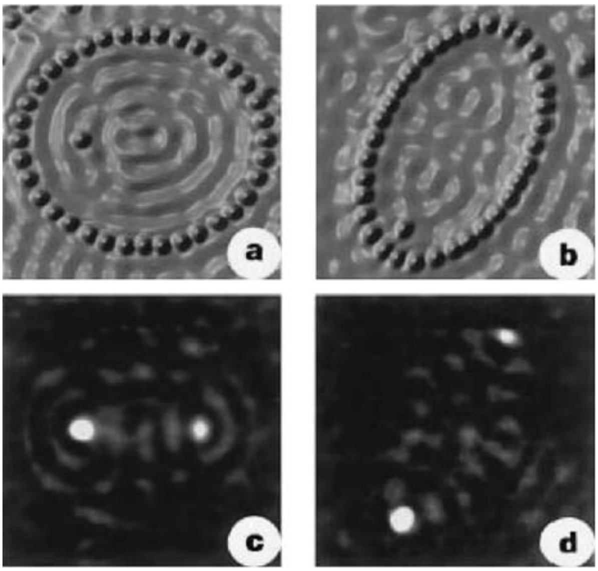

Figure 40. Visualization of the quantum mirage. a, b, Topographs showing the $e = 1/2$ (a) and $e = 0.786$ (b) ellipse each with a Co atom at the left focus. c, d, Associated dI/dV difference maps showing the Kondo effect projected to the empty right focus, resulting in a Co atom mirage. (From Ref. 81)

is switched on and off. In each period of this switching, the classical path length $2a$ changes by a half Fermi wavelength [81].

Because the quantum mirage effect projects information using the wave nature of electrons rather than a wire, it has the potential to enable data transfer within future nanometer scale electronic circuits so small that conventional wires do not work.

4.2. STM Induced Chemical Reaction at Tip

The finely focused electron beam from STM tip can also be used to induce local chemical reaction, which provides another method to fabricate various pre-designed nano-structures on the surface.

In 1992, Dujardin *et al.* demonstrated that individual $B_{10}H_{14}$ molecule adsorbed on Si(111)7 × 7 surface could be dissociated by electrons emitted from STM tip at a bias voltage of 8 V [77]. In 1997, Stipe *et al.* dissociated single O_2 molecules on the Pt(111) surface in the temperature range of 40 to 150 K using tunneling current from an STM tip [82]. Fig. 41 shows that two O_2 molecules are dissociated by voltage pulses of 0.3 V. The dissociation rate as a function of current was found to vary as $I^{0.8\pm0.2}$, $I^{1.8\pm0.2}$, and $I^{2.9\pm0.3}$ for sample biases of 0.4, 0.3, and 0.2 V, respectively. These rates are explained using a general model for dissociation induced by intramolecular vibrational excitations via resonant inelastic electron tunneling [82].

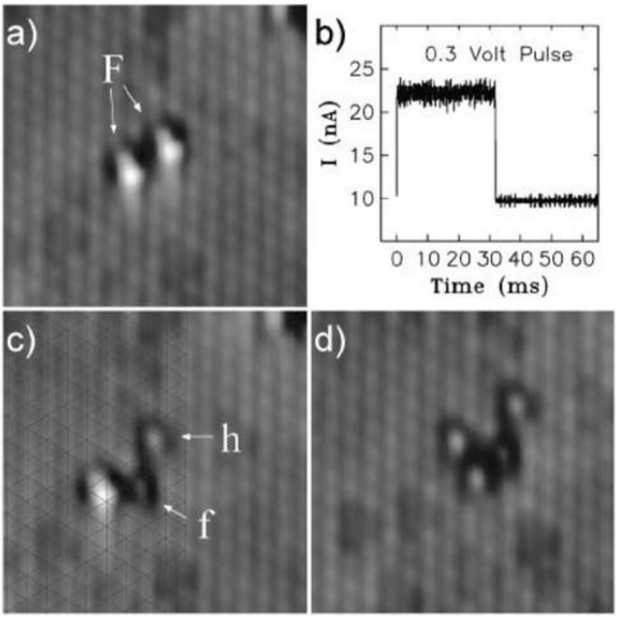

Figure 41. (a) STM image of two adjacent pear shaped O2 molecules on fcc sites. (b) Current during a 0.3 V pulse over the molecule on the right showing the moment of dissociation (step at $t \sim 30$ ms). (c) After pulse image with a grid fit to the platinum lattice showing one oxygen atom on an fcc and one on an hcp site along with the unperturbed neighboring molecule on an fcc site. (d) STM image taken after a second pulse with the tip centered over the molecule showing two additional oxygen atoms on hcp sites. Raw data images scanned at 25 mV sample bias and 5 nA tunneling current. (From Ref. 82)

Recently, it was demonstrated that with an STM in a controlled step-by-step manner utilizing a variety of manipulation techniques, all elementary steps of a complex chemical reaction can be induced on individual molecules and new individual molecules can be synthesized [83]. The reaction steps involve the separation of iodine from iodobenzene by using tunneling electrons, bringing together two resultant phenyls mechanically by lateral manipulation and, finally, their chemical association to form a biphenyl molecule mediated by excitation with tunneling electrons. The reaction process is schematically illustrated in Fig. 42.

The first reaction step, iodine abstraction from iodobenzene [Figs. 42(a) and 1(b)], was performed by positioning the STM tip right above the molecule at fixed height and switching the sample bias to 1.5 V for several seconds. From the linear dependence of the dissociation rate on the tunneling current, they concluded that the energy transfer from a single electron causes the breaking of the C-I bond [83]. As shown in Fig. 43, after dissociation (a–b), the iodine and phenyl are spaced closely (c). So, the iodine atoms were pulled by the tip to further separate them from the phenyls (d). To clear the manipulation path (e), the iodine atom located between the two

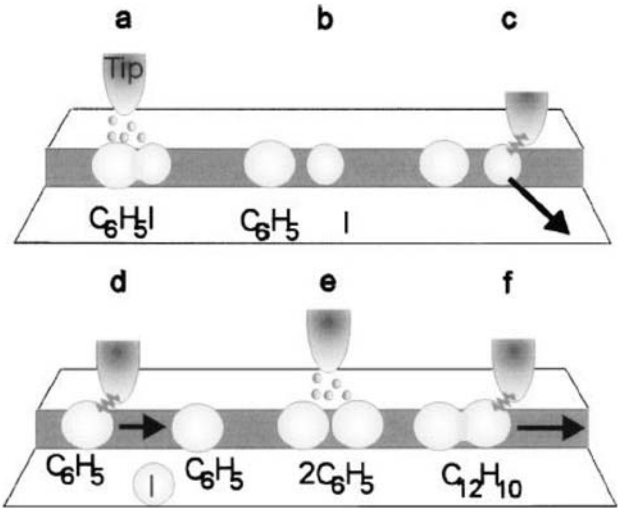

Figure 42. Schematic illustration of the STM tip-induced synthesis steps of a biphenyl molecule. (a), (b) Electron-induced selective abstraction of iodine from iodobenzene. (c) Removal of the iodine atom to a terrace site by lateral manipulation. (d) Bringing together two phenyls by lateral manipulation. (e) Electroninduced chemical association of the phenyl couple to biphenyl. (f) Pulling the synthesized molecule by its front end with the STM tip to confirm the association. (From Ref. 83)

phenyls is removed onto the lower terrace. Lateral manipulation was continued until two phenyls were located close to each other (f). The shortest achievable distance between the centers of two phenyls is 3.9 ± 0.1 Å, as determined from the STM images. Even though the two phenyls are brought together spatially they do not join at the temperature of 20 K unless further measures are taken. To induce the last reaction step, association, molecular excitation by inelastic tunneling was used. The STM tip was stopped right above the center of the phenyl couple and the bias was raised to 500 mV for 10 s. Then the voltage was reduced to its original value of 100 mV and the STM tip continued scanning. The distance between the phenyl centers changes upon association with 4.4 ± 0.05 Å, which is consistent with the distance of 4.3 Å between the two centers of the p rings in gas-phase biphenyl [83].

This work opens up new fascinating routes to the individual assembly of novel man-designed molecules or construction of nanoscale molecular-electronic and molecular-mechanical devices from a variety of building blocks which might also be prepared *in situ*.

More recently, Moresco *et al.* showed that STM tip could be used to rotate single legs of a single Cu-tetra-3,5 *di-terbutyl-phenyl porphyrin* (Cu-TBPP) molecule in and out of the porphyrin plane in a reversible way on a stepped Cu(211) surface [84] and they found the internal configuration modification drastically changed the tunneling current passing through the molecule. This work demonstrated that the controlled

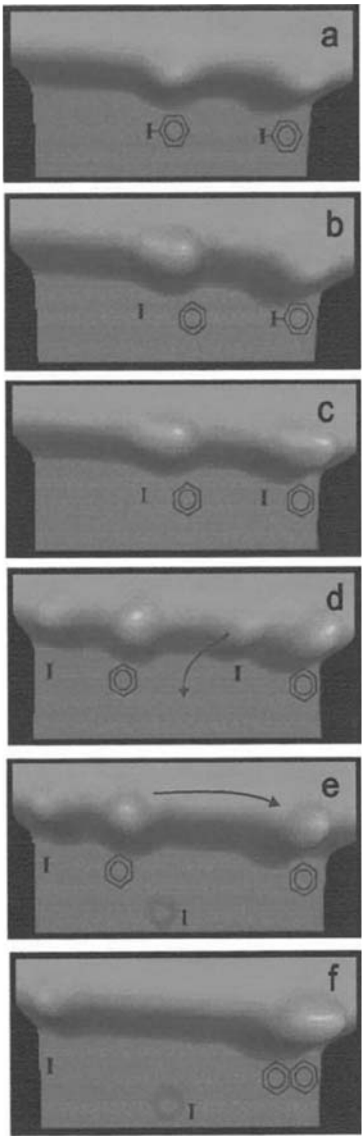

Figure 43. STM images showing the initial steps of the tip-induced Ullmann synthesis. (a) Two iodobenzene molecules are adsorbed at a Cu(111) step edge. (b),(c) Iodine is abstracted from both molecules using a voltage pulse. (d) Iodine atoms (small protrusions) and phenyl molecules (large) are further separated by lateral manipulation. (e) The iodine atom located between the two phenyls is removed onto the lower terrace to clear the path between the two phenyls. (f) The phenyl molecule at the left side is moved by the STM tip close to the right phenyl to prepare for their association. (Image parameters: +100 mV, 0.53 nA; 70 × 30 Å^2.) (From Ref. 83)

rotation of the legs induced by the STM tip realizes the principle of a conformational molecular switch [84].

5. RECENT DEVELOPMENTS

In traditional surface analysis techniques, the sample is probed by means of electrons, photons, ions, and other particles with a spatial resolution determined by the spatial extent of the probe beams. Therefore, atomic resolution is very difficult to achieve with the conventional techniques. In contrast, with atomic-resolution, STM is based on a totally different principle, in which a local probe (very sharp tip), precise scanning, and an electronic feedback are combined subtly. To achieve the atomic resolution, the tip is brought very close to the sample, in near-field regime, and is controlled precisely by monitoring the tunneling current. Following the basic idea of STM, many novel scanning probe microscopes have emerged based on the piezoelectric scanning, feedback control and various interactions between probe tip and sample. Some important techniques have been summarized in Table I by Wickramasinghe [5]. Below, some current developments will be reviewed.

5.1. Spin-Polarized STM (SPSTM)

In the STM/STS discussed above, the spin of the tunneling electrons has not been considered. If a magnetic tip is used, the tunneling current will be spin-dependent. This means that the STM tip is sensitive to the spin of the tunneling electrons and can be used to investigate the magnetism structure of a sample with high spatial resolution. This idea was first proposed by Pierce in 1988 [85] and it eventually led to the invention of the spin-polarized STM (SPSTM).

For SPSTM, a magnetic tip is required to provide a highly efficient source or detector for spin-polarized (SP) electrons. The ideal tip for SPSTM must meet several conditions: First of all, the apex atom must exhibit a high spin polarization in order to achieve a good signal-to-noise ratio. Second, dipolar interaction between tip and sample due to the stray fields should be as low as possible because it may modify or destroy the intrinsic domain structure of the sample. Third, in order to separate magnetic from topographic and electronic contributions to the tunnel current it should be possible to reverse the quantization axis periodically. Finally, in order to be able to image the domain structure of any sample-no matter whether its easy axis is in-plane or out-of-plane, one should be able to control the orientation of the quantization axis of the tip parallel or perpendicular to the sample surface [86]. Several possible tip materials have been discussed in Ref. 4. The details on how to prepare an SPSTM tip can be found in Ref. 86. In the following, some applications of SPSTM are reviewed.

Using CrO_2 tip and a Cr(001) sample, Weisendanger *et al.* observed the vacuum tunneling of SP electrons in SPSTM for the first time in 1990 [87]. The topological antiferromagnetism of the Cr(001) surface with terraces alternately magnetized in opposite directions and separated by monatomic steps provides an ideal test structure for SPSTM experiments. With a normal nonmagnetic W tip, the monatomic step

Table I. SXM Techniques and Capabilities (From Ref. 5)

1. Scanning Tunneling Microscope (1981)
   –G. Binnig, H. Rohrer
   –Atomic resolution images of conducting surfaces
2. Scanning Near-Field Optical Microscope (1982)
   –D. W. Pohl
   –50 nm (lateral resolution) optical images
3. Scanning Capacitance Microscope (1984)
   –J. R. Matey, J. Blanc
   –500 nm (lat. res.) images of capacitance variation
4. Scanning Thermal Microscope (1985)
   –C. C. Williams, H. K. Wickramasinghe
   –50 nm (lat. res.) thermal images
5. Atomic Force Microscope (1986)
   –G. Binning, C. F. Quate, Ch. Gerber
   –Atomic resolution on conducting/nonconducting surfaces
6. Scanning Attractive Force Microscope (1987)
   –Y. Martin, C. C. Williams, H. K. Wickramasinghe
   –5 nm (lat. res.) non-contact images of surfaces
7. Magnetic Force Microscope (1987)
   –Y. Martin, H. K. Wickramasinghe
   –100 nm (lat. res.) images of magnetic bits/heads
8. "Frictional" Force Microscope (1987)
   –C. M. Mate, G. M. McClelland, S. Chiang
   –Atomic-scale images of lateral ("frictional") forces
9. Electrostatic Force Microscope (1987)
   –Y. Martin, D. W. Abraham, H. K. Wickramasinghe
   –Detection of charge as small as single electron
10. Inelastic Tunneling Spectroscopy STM (1987)
    –D. P. E. Smith, D. Kirk, C. F. Quate
    –Phonon spectra of molecules in STM
11. Laser Driven STM (1987)
    –L. Arnold, W. Krieger, H. Walther
    –Imaging by non linear mixing of optical waves in STM
12. Ballistic Electron Emission Microscope (1988)
    –W. J. Kaiser (1988)
    –Probing of Schottky barriers on nm scale
13. Inverse Photoemission Force Microscope (1988)
    –J. H. Coombs, J. K. Gimzewski, b. Reihl, J. K. Sass, R. R. Schlittler
    –Luminescence spectra on nm scale
14. Near Field Acoustic Microscope (1989)
    –K. Takata, T. Hasegawa, S. Hosaka, S. Hosoki, T. Komoda
    –Low frequency acoustic measurements on 10 nm scale
15. Scanning Noise Microscope (1989)
    –R. Moiler, A. Esslinger, B. Koslowski
    –Tunneling microscopy with zero tip-sample bias
16. Scanning Spin-precession Microscope (1989)
    –Y. Manassen, R. Hamers, J. Demuth, A. Castellano
    –1 nm (lat. res.) images of paramagnetic spins
17. Scanning Ion-Conductance Microscope (1989)
    –P. Hansma, B. Drake, O. Marti, S. Gould, C. Prater
    –500 nm (lat. res.) images in electrolyte

(continued)

Table I. (continued)

18. Scanning Electrochemical Microscope (1989)
    −O. E. Husser, D. H. Craston, A. J. Bare
19. Absorption Microscope/Spectroscope (1989)
    −J. Weaver, H. K. Wickramasinghe
    −1 nm (lat. res.) absorption images/spectroscopy
20. Phonon Absorption Microscope (1989)
    −H. K. Wickramasinghe, J. M. R. Weaver, C. C. Williams
    −Phonon absorption images with nm resolution
21. Scanning Chemical Potential Microscope (1990)
    −C. C. Williams, H. K. Wickramasinghe
    −Atomic scale images of chemical potential variation
22. Photovoltage STM (1990)
    −R. J. Hamers, K. Markert
    −Photovoltage images on nm scale
23. Kelvin Probe Force Microscope (1991)
    −M. Nonnenmacher, M. P. O'Boyle, H. K. Wickramasinghe
    −Contact potential measurements on 10 nm scale

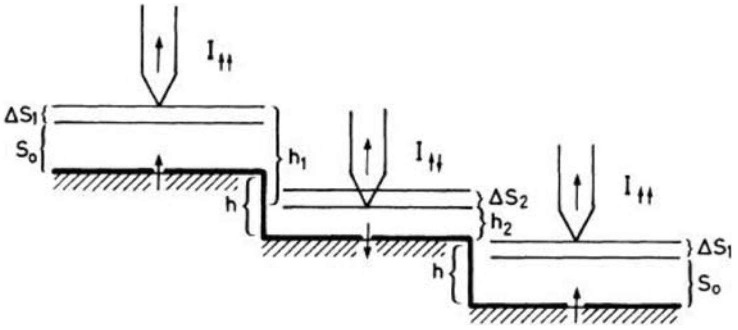

Figure 44. Schematic drawing of a ferromagnetic tip scanning over alternately magnetized terraces separated by monatiomic steps of height h. An additional contribution from SP tunneling leads to alternating step heights $h_1 = h + \Delta s_1 + \Delta s_2$ and $h_2 = h - \Delta s_1 - \Delta s_2$. (From Ref. 87)

height of Cr(001) was determined to be 1.49 ± 0.08 Å from STM topographic images, which is in good agreement with 1.44 Å for bcc Cr(001). The CrO_2 tip was prepared in such a way that the preferred magnetization direction of the tip is perpendicular to the sample surface [87]. After replacing the W tip by a CrO_2 tip, a periodic alternation of the measured monatomic step heights between larger and smaller values compared to the mean single step height value of 1.44 Å is observed. The deviation from the single step height value determined with a CrO_2 tip can be as large as ±15% which is much larger than the experimental error with a nonmagnetic W tip. An additional contribution from SP tunneling was employed to explain the periodic alternation of the monatomic step height values. As sketched in Fig. 44, assuming that the CrO_2 tip is first scanning over a terrace with the same direction of magnetization as the CrO_2

tip, the tunneling current $I_{\uparrow\uparrow}$ will then be increased due to a contribution from SP tunneling: $I_{\uparrow\uparrow} = I_0(1 + P)$, where I_0 is the tunneling current without this contribution and P is the effective spin polarization of the tunneling junction. Since the STM is operated at constant current, an additional contribution to the tunneling current leads to a corresponding increase Δs_1 of the mean distance s_0 between the tip and the sample surface. If the CrO_2 tip is scanning over a terrace with the opposite direction of magnetization, the tunneling current $I_{\uparrow\downarrow}$ will be decreased: $I_{\uparrow\downarrow} = I_0(1-P)$, leading to a corresponding decrease Δs_2 of the tip-sample distance. The measured single step height values therefore alternate between $h_1 = h + \Delta s_1 + \Delta s_2$ and $h_2 = h - \Delta s_1 - \Delta s_2$, where h is the topographic monatomic step height.

The effective polarization of the tunneling junction is given by [Ref. 87]:

$$P = \frac{I_{\uparrow\uparrow} - I_{\uparrow\downarrow}}{I_{\uparrow\uparrow} + I_{\uparrow\downarrow}} = \frac{\exp(A\sqrt{\phi}\Delta s_1) - \exp(-A\sqrt{\phi}\Delta s_2)}{\exp(A\sqrt{\phi}\Delta s_1) + \exp(-A\sqrt{\phi}\Delta s_2)} = \frac{\exp(A\sqrt{\phi}\Delta s) - 1}{\exp(A\sqrt{\phi}\Delta s) + 1}, \tag{18}$$

where $A \approx 1.025\ \mathrm{eV}^{-1/2}\ \text{Å}^{-1}$, ϕ is the average local tunneling barrier height, $\Delta s = \Delta s_1 + \Delta s_2$. According to the experimental results, $\Delta s = 0.2 \pm 0.1$ Å, taking $\phi = 4.0 \pm 0.5$ eV, the effective polarization of the tunneling junction P was derived to be $(20 \pm 10)\%$.

The first SPSTM studies of the Cr(001) surface were performed on a nanometer scale. The CrO_2 tips were too blunt to achieve atomic resolution. The first atomic resolution SPSTM experiment was done on $Fe_3O_4(001)$ surface. The different spin configurations of $3d^{5\uparrow}3d^{\downarrow}$ for Fe^{2+} and $3d^{5\uparrow}$ for Fe^{3+} were identified by using a sharp Fe tip prepared *in situ* [88, 89].

Real-space imaging of two-dimensional antiferromagnetism with the atomic resolution was achieved also by Wiesendanger's group in 2000 [90]. The experiment was done on Mn/W(110) surface with an SPSTM at 16 K. A monolayer Mn grows pseudomorphically on W(110) surface. An STM image with W tip is shown in Fig. 45(A). First-principles calculations shows that the so-called c(2 × 2) antiferromagnetic state is energetically favourable and that the magnetocrystalline anisotropy energy favours an in-plane spin orientation. In SPSTM experiments, Fe-coated probe tips was used to fulfill the condition that the experiment required a magnetic tip with a magnetization axis in the plane of the surface. Figure 45(B) shows an STM image taken with such a tip. Periodic parallel stripes along the [001] direction of the surface can be recognized. The periodicity along the [110] direction amounts to 4.5 ± 0.1 Å, which corresponds well to the size of the magnetic c(2 × 2) unit cell. The inset in Fig. 45(B) shows the calculated STM image for the magnetic ground state, i.e., the c(2 × 2)-AFM configuration. The theory and experiment are in a very good agreement [86, 90].

These stuties demonstrate that SPSTM is a powerful technique for understanding of complicated magnetic configurations of nanomagnets and thin films engineered from ferromagnetic and antiferromagnetic materials used for magnetoelectronics.

Recently, it was demonstrated that SPSTM images can be observed with an antiferromagnetic probe tip. The advantage of its vanishing dipole field is most apparent

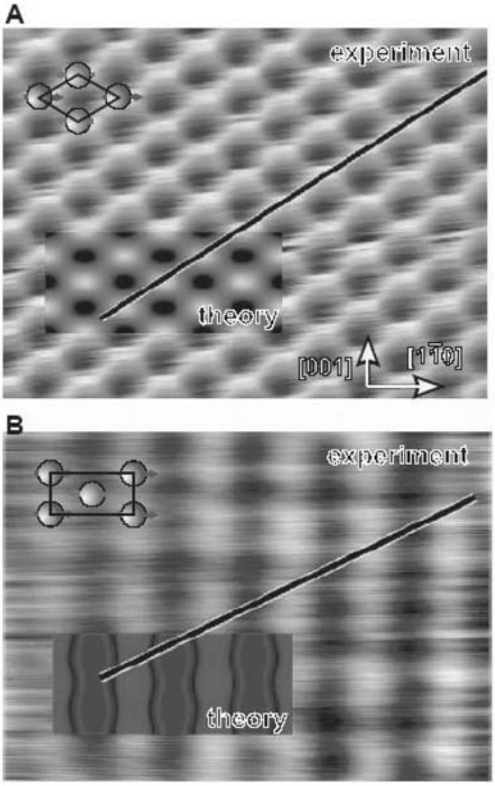

Figure 45. Comparison of experimental and theoretical STM images of a Mn ML on W(110) with (A) a nonmagnetic W tip and (B) a magnetic Fe tip. The unit cell of the calculated magnetic ground-state configuration is shown in (A) and (B) for comparison. Tunneling parameters for both images are $I_t = 40$ nA and $U = 23$ mV. The image size is 2.7 nm by 2.2 nm. (From Ref. 90)

in external magnetic fields. This new approach resolves the problem of the disturbing influence of a ferromagnetic tip in the investigation of soft magnetic materials and superparamagnetic particles [91].

In order to overcome the difficulties of separating topographic, electronic, and magnetic information one may measure the local differential conductivity dI/dV with a magnetic tip [86]. In Fig. 46, the dI/dV spectra measured on Gd(0001) at a sample temperature $T = 170$ K is compared with (inverse) photoemission spectroscopy (IPES) data on a similar sample at the same temperature. It is known from previous experiments that the Gd(0001) surface state is exchange-split into a filled majority and an empty minority spin contribution. While the occupied majority spin part (↑) appears as a peak in the PES data the unoccupied minority spin part (↓) is observed in IPES measurements. Indeed, tunneling dI/dV spectra exhibit a peak at a sample bias value of $V = +430$ mV and a shoulder at $V = -200$ mV (Fig. 46, top panel), being in

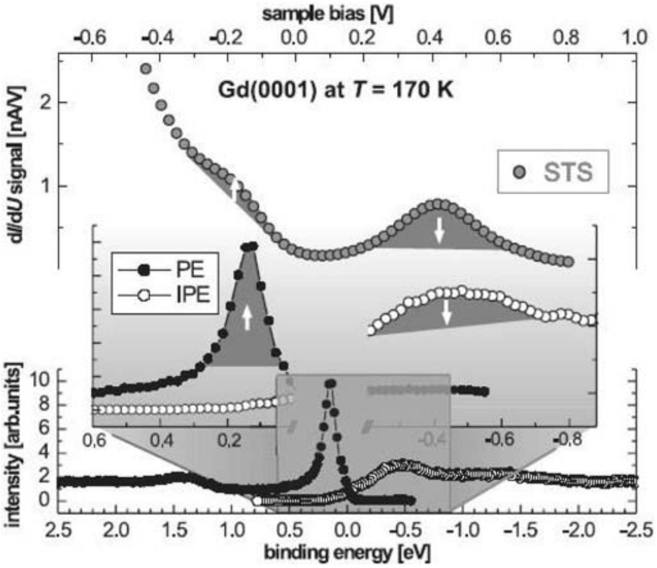

Figure 46. PE (left) and IPE (right) spectra of the spin-split Gd(0001) surface state measured at 170 K (bottom panel). The occupied part of the surface state appears in the PES while the empty part is weakly visible in the IPES (bottom and inset). In contrast, tunnelling spectroscopy allows the measurement of occupied and empty electronic states within a single experiment (top). The peak position derived with both experimental techniques correspond well. (From Ref. 86)

good agreement with the binding energies for the empty and the occupied parts of the surface state as determined by PES and IPES (see Fig. 46, bottom panel).

dI/dV mapping with nanometer resolution can be also performed with a magnetic tip. Fig. 47 shows the STM topographic image and spatially resolved $\mathrm{d}I/\mathrm{d}V$ images measured at $T = 70$ K with a W tip coated with 5–10 ML Fe on a sample prepared by depositing 10 ML of Gd on the W(110) substrate held at 530 K. This preparation procedure leads to partially coalesced Gd islands ($\theta_{\mathrm{loc}} \approx 20$ ML) with a single Gd wetting layer on the W(110) substrate as shown in the STM image of Fig. 47(a). Fig. 47(b) and (c) show dI/dV images at $V = -0.2$ V and $+0.45$ V, i.e. sample biases which correspond to filled and empty parts of the surface state, respectively, measured within the box of Fig. 47(a). Both images show a domain wall crossing the island from top to bottom [86, 92]. This work demonstrates that the domain structure of Gd(0001) islands with a resolution below 20 nm can be imaged by dI/dV mapping with a magnetic tip.

Recently, Wulfhekel and Kirschner showed that magnetic contrast could be obtained in a similar way of measuring the tunnel magnetoresistance (MR) of planar junctions [93]. By applying an alternating current of frequency f through a small coil wound around the magnetic tip, the longitudinal magnetization of the tip was switched periodically. The tip material, a metallic glass, was chosen to have a low coercivity, vanishing

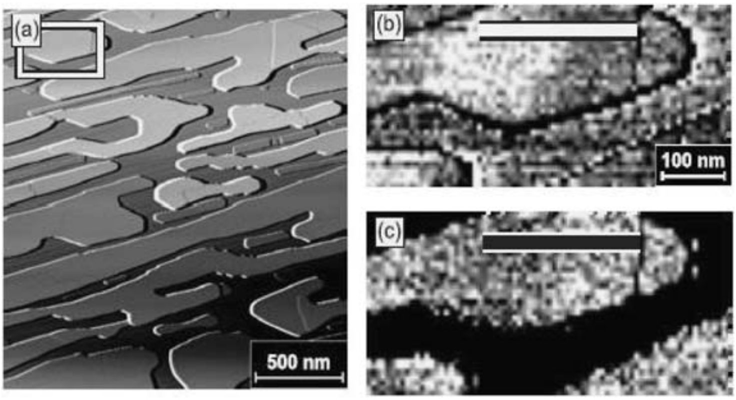

Figure 47. (a) Topographic image of 10 ML Gd(0001)/W(110). dI/dU maps measured on the island indicated by the box in (a) at (b) $U = -0.2$ V and (c) $U = +0.45$ V, i.e. the peak position of the majority and minority parts of the surface state, respectively. In (b) the left part of the island appears brighter (high conductivity) than the right part (low conductivity). In (c) the contrast is reversed. (From Ref. 86)

magnetostriction, low saturation magnetization, and low magnetization losses. These parameters allow a rapid switching of the magnetization of the tip without mechanical vibrations of the tip due to magnetostriction or magnetization losses. Furthermore, they minimize the influence of the field of the coil on the sample magnetization. The frequency f was chosen far away from any mechanical resonances of the STM and well above the cutoff frequency of the feedback loop. Variations of the tunnel probability due to the magnetotunnel effect, i.e., maximal probability for parallel and minimal for antiparallel orientation between tip and sample magnetization, result in variations of the tunnel current with the frequency f. These variations were detected with a lock-in amplifier. Since the tip is magnetized along its axis and perpendicular to the sample surface, sensitivity for the perpendicular magnetic component of the sample was obtained [93]. In contrast to the previously described spectroscopy of the differential conductivity dI/dV, which requires that different domains are simultaneously visible in a single image this dI/dm_T method allows the identification of a magnetic contrast even if the sample is in a single-domain state. Since the local MR method allows a rather direct detection of the sample's domain structure a detailed knowledge of the spin-averaged electronic structure of the surface under investigation is no longer required [86, 93].

The high spatial resolution and surface magnetic sensitivity of SPSTM allow it be a powerful tool to study the unsolved basic magnetic problems. There is no doubt that SPSTM will play a major role in the field of magnetic microscopy in the following years.

5.2. Ultra-Low Temperature (ULT)-STM

Ultra-low temperature STM (ULTSTM) is an important direction in the development of scanning tunneling microscopes. STM working in the millikelvin temperature range allows the study of physical phenomena that only occur at very low temperatures, for example, superconducting phase transitions in heavy fermion materials. Very low temperatures can also dramatically improve the energy resolution in the STM measurements. In, 1999, Pan *et al.* succeeded in building an ULTSTM for operation in a magnetic field with very high spatial and spectroscopic resolution [94].

Although low temperatures bring the benefits of low thermal drift and low thermal noise, which are required for high-resolution measurements, ultra-low temperature refrigeration techniques often hamper the efforts to achieve high-resolution measurements due to the introduction of mechanical vibrations, e.g. vibrations due to evaporation of the liquid, and from pumps. Furthermore, the physical space within the cryostat, especially when a high magnetic field is required, is often too limited to allow an effective cryogenic vibration-isolation stage. Therefore, to design an ULTSTM which can achieve atomic resolution is challenging. These challenges were overcome by the efforts in the following three elements: (1) a very rigid STM head that is less susceptible to vibration, (2) a refrigeration scheme that has very low intrinsic vibrational noise, and (3) a good external vibration-isolation system to reduce transmission of vibrations from the external environment to the STM cryostat. Finally, they demonstrated that the ^{3}He refrigerator based very low temperature STM they constructed can reliably operate at temperatures down to 250 mK and in magnetic fields of up to 7 T with high spatial and spectroscopic resolution.

Recently, a dilution-refrigerator-based STM with sample temperatures of 20 mK was achieved [95]. The unconventional superconductor, $Sr_2Ti_xRu_{1-x}O_4$ with $x = 0.00125$, was studied with this ULTSTM. Fig. 48(a) shows an atomic resolution topographic image of the SrO plane of Ti-doped Sr_2RuO_4 with the square lattice of Sr atoms clearly visible. The four dark spots correspond to the Ti atoms replacing the Ru atoms one layer below the surface. A complicated gap-like structure in local density of states was measured at all locations on the surface, with some modifications caused by the Ti atoms. The superconducting gap was not clearly visible, possibly due to surface termination effects, but other gap-like structures were found at ~5 and ~50 meV [95].

5.3. Dual-tip STM

Dual-tip STM (DTSTM) was first suggested by Niu *et al.* [96] in 1995. Normal single-tip STM can only probe static properties of electronic system, the transport properties are out of its capability. A DTSTM can solve this problem easily. Niu *et al.* also proposed that a DTSTM can be applied to: (1) deduce useful information about the band structure of surface states; (2) measure scattering phase shifts of surface defects; (3) observe transition from ballistic to diffusion transport to localization; and (4) measure inelastic mean free paths [96].

Actually, Tsukamoto *et al.* had built a twin-tip STM in 1991. However, the two tips were fixed together and could not scan independently [97]. In 2001, Watanabe *et al.* reported that they had constructed a DTSTM using multiwall carbon nanotubes (NT) as STM probes. They also developed an active damper system for DTSTM to reduce

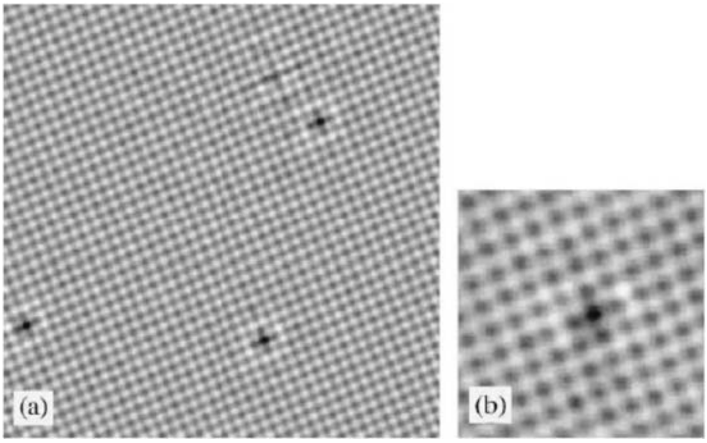

Figure 48. Topographic image of $Sr_2Ti_xRu_{1-x}O_4$ where $x = 0.00125$. The white lattice is the SrO plane, and the black cross-like objects are the Ti atoms located one layer below the surface. (a) 120 Å x 120 Å image, (b) enlarged (35 Å square) view of single impurity. (Images taken at 0.1 nA and −100 mV). (From Ref. 95)

mechanical vibration, which is dominated by the characteristic vibration of the two-probe system. The DTSTM allows to elucidate the electric property of a sample with a spatial resolution of ~1 nm. Using this system, the current–voltage curves of a single NT ring have been measured. The electrode configuration is shown in Fig. 49(a). Fig. 49(b) shows a DTSTM constant current image of the NT ring and the first probe. The I–V curves for various V_G (0, 1, 2, 3, 4, and 5 V, respectively) measured by DTSTM at room temperature in dry-N_2 atmosphere are shown in Fig. 49(c). These results show that the small NT ring on the Si substrate is a field-effect transistor having sharp switching behavior and the possibility of nanometer-scale electronic circuits composed of NT devices [98].

Also in 2001, an ultra-high vacuum DTSTM with two mechanically and electrically independent probes was built by Boland's group [99].

Meanwhile, an ultrahigh vacuum compatible cryogenic DTSTM was constructed by Chen's group [100]. The microscope is attached at the bottom of a low-loss liquid helium Dewar and can be operated down to 4.2 K. The two tips can be manipulated independently and positioned as close as one desires limited only by their radius of curvature. The coarse positioning system consists of five linear steppers driven by piezo-tubes. The displacement of each stepper can be monitored by its own embedded capacitive position sensor with a submicron resolution, thus allowing accurate control of the tip navigation process. An alignment procedure, using a specimen made of three mutually nonparallel planes, is introduced to bring the two tips into overlapped scan ranges without the help of an additional guiding device such as an electron microscope. The overall system exhibits good mechanical rigidity and atomic resolution

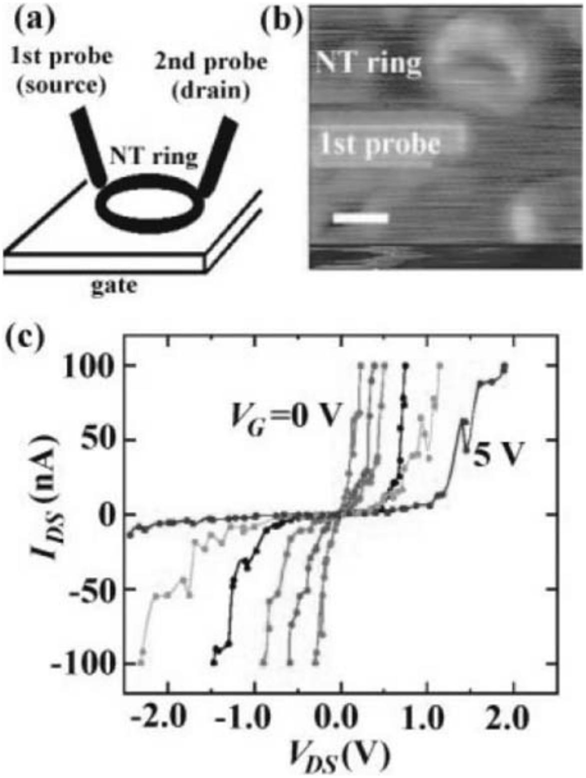

Figure 49. (a) Electrode configuration: two NT probes were connected with a NT ring on the poly-Si($\sim$3.5 nm, *n*-type)/SiO$_2$ ($\sim$2 nm)/Si(100)/Au substrate, where the Au layer acted as a gate electrode. (b) The DTSTM constant current image of the NT ring and the first probe (scale bar, 10 nm). The image was recorded by scanning the second probe. (c) I–V curves for various V_G measured by DTSTM at room temperature in dry-N$_2$ atmosphere. V_G from left to right are 0, 1, 2, 3, 4, and 5 V, respectively. (From Ref. 98)

has been achieved with either tip. This instrument is well suited for investigating low temperature quantum properties of atomically clean nanostructures in a three-terminal configuration [100].

We have reason to believe that, with the fast development of DTSTMs, they will play more important roles in the research of surface science, nano-materials, nano-devices and *etc.*

5.4. Variable Temperature Fast-Scanning STM

STM has been proved to be very successful in studies of the static structural or electronic properties of surfaces. However, it is often desirable to investigate dynamic processes, i.e., surface diffusion, chemical reactions, nucleation and growth, or phase

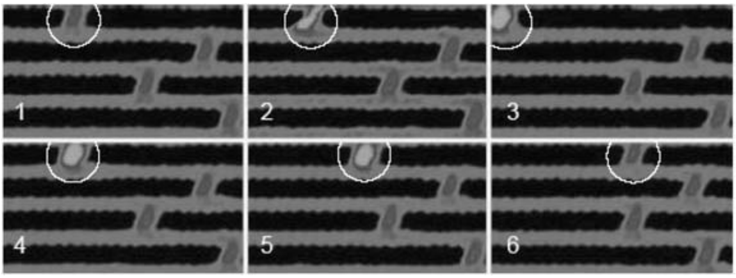

Figure 50. Six STM images (56 × 31 Å^2) extracted from a typical STM movie. Shown is the development of a normal Pt adatom into a bright Pt-H intermediate complex, and then back to a normal Pt adatom again. All STM images were obtained in the constant-current mode with tunnel resistances above 100 MΩ in which case the influence of the tip was found to be negligible. The Pt adatom of interest is marked by a white circle. (From Ref. 110)

transformations. Therefore, high-speed STM is needed for these applications. Since temperature influences the rate of such kinetic processes strongly, control of the sample temperature may allow one to adjust the rate for the processes to the accessible time scale of the STM. Thus, a variable temperature fast-scanning STM is a unique tool to observe dynamic processes. Many variable temperature fast-scanning STMs have been developed in various groups [101–108] with the scanning speed up to 20 frames/s [103], and temperature range from 25 K to 900 K (each instrument can only change temperature in a different smaller range). To achieve the high scanning speed, constant-height scanning mode is often used [103].

A lot of successful applications have been performed with variable temperature fast-scanning STMs.

The one-dimensional diffusion of Pt adatoms in the missing row troughs of the reconstructed Pt(110)(1 × 2) surface is monitored directly from atomically resolved fast-scanning STM images by Besenbacher's group [109]. It is found that not only jumps between nearest neighbor sites but also long jumps, i.e., jumps between next nearest neighbor sites, take place. The hopping rate for these long jumps is found to follow an Arrhenius dependence on temperature. The activation barriers for single and double jumps are determined to be $E_{d1} = -0.81$ eV and $E_{d2} = -0.89$ eV, respectively. This energy difference may be interpreted as a measure of the energy dissipation of the Pt adatoms on the Pt(110)-(1 × 2) surface [109].

Later, they also found that surface self-diffusion of Pt adatoms can be enhanced by adsorbed hydrogen and observed the formation of Pt-H complex which has a diffusivity enhanced by a factor of 500 at room temperature, relative to the other Pt adatoms [110]. As shown in Fig. 50, the formation of intermediate Pt-H complexes has been directly imaged by a fast-scanning STM at 303 K and a hydrogen pressure of 7×10^{-7} mbar. These Pt-H complexes show up in the STM images as brighter Pt adatoms (increase in apparent height ~0.4 Å). After some time, the brighter adatom reverts to a normal brightness. The density functional calculations indicated that the

Pt-H complex consists of a hydrogen atom trapped on top of a platinum atom, and that the bound hydrogen atom decreases the diffusion barrier.

The catalytic oxidation of carbon monoxide (CO) on a platinum (111) surface was studied by Ertl's group with a variable temperature fast-scanning STM [111]. The adsorbed oxygen atoms and CO molecules were imaged with atomic resolution, and their reactions to carbon dioxide (CO_2) were monitored as functions of time. From temperature dependent measurements, they obtained the kinetic parameters, which agree well with the data from macroscopic measurements. In this way, kinetic description of a chemical reaction was achieved that is based solely on the statistics of the underlying atomic processes observed by STM.

Traveling reaction fronts in the oxidation of hydrogen on a Pt(111) surface were also investigated by them [112–113]. These fronts were observed during dosing of the oxygen-covered surface with hydrogen at temperatures below 170 K. The fronts represented 10 to 100 nm wide OH-covered regions, separating unreacted O atoms from the reaction product H_2O. O atoms were transformed into H_2O by the motion of the OH zone. Their investigations revealed the velocity and the width of the fronts as a function of temperature. A simple reaction–diffusion model has been constructed, which contains two reaction steps and the surface diffusion of water molecules, and qualitatively reproduces the experimental observations.

REFERENCES

1. G. Binnig, H. Rohrer, Ch. Gerber, and E. Weibel, Phys. Rev. Lett. **49**, 57 (1982).
2. J. Bardeen, Phys. Rev. Lett. **6**, 57 (1961).
3. J. Tersoff and D. R. Hamann, Phys. Rev. Lett. **50**, 1998 (1983) and Phys. Rev. **B31,** 805 (1985).
4. R. Wiesendanger, "Scanning probe microscopy and spectroscopy-methods and applications" Cambridge University Press, 1994.
5. J. A. Stroscio, W. J. Kaiser, "Scanning tunneling microscopy", Academic Press, 1993.
6. C. J. Chen, "Introduction to scanning tunneling microscopy", Oxford University Press, 1993.
7. R. E. Schlier and H. E. Farnsworth, J. Chem. Phys. **30**, 917 (1959).
8. K. Takayanagi, Y. Tanishiro, M. Takahashi and S. Takahashi, J. Vac. Sci. Technol. **A3**, 1502 (1985).
9. A. T. Cho, J. Appl. Phys., **47**, 2841 (1976).
10. H. H. Farrel and C. J. Palmstrom, J. Vac. Sci. Technol. **B8**, 903 (1990).
11. D. J. Chadi, J. Vac. Sci. Technol. **A5**, 834 (1987).
12. J. E. Northrup, and S. Froyen, Phys. Rev. Lett. **71**, 2276 (1993).
13. T. Hashizume, Q. K. Xue, J. M. Zhou, A. Ichimiya, and T. Sakurai, Phys. Rev. Lett. **73**, 2208 (1994).
14. T. Hashizume, Q. K. Xue, A. Ichimiya, and T. Sakurai, Phys. Rev. **B51**, 4200 (1995).
15. Q. K. Xue, T. Hashizume, J. M. Zhou, T. Sakata, T. Ohno, and T. Sakurai, Phys. Rev. Lett. **74**, 3177 (1995).
16. S. H. Lee, W. Moritz, and M. Scheffler, Phys. Rev. Lett. **85**, 3890 (2000).
17. D. Paget, Y. Garreau, M. Sauvage, P. Chiaradia, R. Pinchaux, and W. G. Schmidt, Phys. Rev. B 64, R161305 (2001); C. Kumpf, L. D. Marks, D. Ellis, D. Smilgies, E. Landemark, M. Nielsen, R. Feidenhans'l, J. Zegenhagen,O. Bunk, J. H. Zeysing, Y. Su, and R. L. Johnson, Phys. Rev. Lett. **86**, 3586 (2001); W. G. Schmidt, F. Bechstedt, and J. Bernholc, Applied Surface Science **190**, 264 (2002); W. G. Schmidt, Appl. Phys. **A 75**, 89 (2002); M. Pristovsek, S. Tsukamoto, A. Ohtake, N. Koguchi, B. G. Orr, W. G. Schmidt, and J. Bernholc, Phys. Stat. Sol. **240**, 91 (2003).
18. S. Nakamura, T. Mukai, M. Senoh, Appl. Phys. Lett. **64**, 1687 (1994).
19. R. Smith, R. M. Feenstra, D. W. Greve, J. Neugebauer, and J. Northrup, Phys. Rev. Lett. **79**, 3934 (1997).
20. A. R. Smith, R. M. Feenstra, D. W. Greve, M.-S. Shin, M. Skowronski, J. Neugebauer, and J. Northrup, Appl. Phys. Lett. **72**, 2114 (1999).

21. Q. K. Xue, Q. Z. Xue, R. Z. Bakhtizin, Y. Hasegawa, I. S. T. Tsong, T. Sakurai, and T. Ohno, Phys. Rev. Lett. **82**, 3074 (1999).
22. V. Ramachandran *et al.,* preceding Comment, Phys. Rev. Lett. **84**, 4014 (2000).
23. A. R. Smith, R. M. Feenstra, D. W. Greve, M. S. Shin, M. Skowronski, J. Neugebauer, and J. E. Northrup, J. Vac. Sci. Technol. B **16**, 2242 (1998).
24. A. R. Smith, R. M. Feenstra, D. W. Greve, M. S. Shin, M. Skowronski, J. Neugebauer, J. E. Northrup, *Surf. Sci.* **423**, 70 (1999).
25. A. R. Smith, V. Ramachandran, R. M. Feenstra, D. W. Greve, A. Ptak, T. Myers, W. Sarney, L. Salamanca-Riba, M. Shin, M. Skowronski, *MRS Internet J. Nitride Semicond Res.* **3**, 12 (1998).
26. J. E. Northrup, J. Neugebauer, R. M. Feenstra, A. R. Smith, Phys. Rev. B **61**, 9932 (2000).
27. C. Adelmann, J. Brault, D. Jalabert, P. Gentile, H. Mariette, Guido Mula, B. Daudin, J. Appl. Phys. **91**, 9638 (2002).
28. Christoph Adelmann, Julien Brault, Guido Mula, Bruno Daudin, Phys. Rev. B **67**, 165419 (2003).
29. A. R. Smith, R. M. Feenstra, D. W. Greve, J. Neugebauer, and J. E. Northrup, Phys. Rev. Lett. **79**, 3934 (1997).
30. J. L. Li, J. F. Jia, X. J. Liang, X. Liu, J. Z. Wang, Q. K. Xue, Z. Q. Li, J. S. Tse, Z. Y. Zhang, and S. B. Zhang, Phys. Rev. Lett. **88**, 066101 (2002).
31. J. F. Jia, X. Liu, J. Z. Wang, J. L. Li, X. S. Wang, Q. K. Xue, Z. Q. Li, Z. Y. Zhang and S. B. Zhang, Phys. Rev. **B66**, 165412 (2002).
32. J. F. Jia, J. Z. Wang, X. Liu, Q. K. Xue, Z. Q. Li, Y. Kawazoe and S. B. Zhang, Appl. Phys. Lett. **80**, 3186 (2002).
33. M. Y. Lai and Y. L. Wang, Phys. Rev. B **64**, 241404 (2001); V. G. Kotlyar, *et al.*, Phys. Rev. B **66**, 165401 (2002); H. H. Chang, *et al.*, Phys. Rev. Lett. **92**, 066103 (2003); K. Wu, *et al.*, Phys. Rev. Lett. **91**, 126101 (2003).
34. G. Binnig, H. Rohrer, Ch. Gerber, and E. Weibel, Surf. Sci. **131**, L379 (1983).
35. V. M. Hallmark, S. Chiang, J. F. Rabolt, J. D. Swallen, and R. J. Wilson, Phys. Rev. Lett. **59**, 2879 (1987).
36. Ch. Wöll, S. Chiang, R. J. Wilson, and P. H. Lippel, Phys. Rev. **B39**, 7988 (1989).
37. J. A. Stroscio, D. T. Pierce, R. A. Dragoset, and P. N. First, J. Vac. Sci. Technol. **A10**, 1981 (1991).
38. Z. Gai, Y. He, X. Li, J. F. Jia, and W. S. Yang, Surf. Sci. **365**, 96 (1996).
39. E. Umbach, K. Glöckler, and M. Sokolowski, Surf. Sci. **402–404**, 20 (1998).
40. B. Kesemo, Surf. Sci. **500**, 656 (2002).
41. X. Zhao, H. Wang, R. G. Zhao, and W. S. Yang, Mater. Sci. Eng. **C16**, 41 (2001).
42. X. Zhao, H. Yan, R. G. Zhao, and W. S. Yang, Langmuir **18**, 3910 (2002).
43. X. Zhao, R. G. Zhao, and W. S. Yang, Langmuir **16**, 9812 (2000).
44. X. Zhao, R. G. Zhao, and W. S. Yang, Langmuir **18**, 433 (2002).
45. X. Zhao, H. Yan, R. G. Zhao, and W. S. Yang, Langmuir **19**, 809 (2003).
46. X. Zhao, J. Am. Chem. Soc. **122**, 12584 (2000).
47. M. Corso, W. Auwärter, M. Muntwiler, A. Tamai, T. Greber, J. Osterwalder, Science **303**, 219 (2004).
48. W. Hebenstreit, M. Schmid, J. Redinger, R. Podloucky, P. Varga, Phys. Rev. Lett. **85**, 5376 (2000).
49. O. Dulub, U. Diebold, and G. Kresse, Phys. Rev. Lett. **90**, 016102 (2003).
50. D. A. Bonnell, Prog. in Surf. Sci. **57**, 187 (1998).
51. K. Bobrov, A. J. Mayne, and G. Dujardin, Natrue **413**, 616 (2001).
52. S. Iijima, Nature **354**, 56 (1991).
53. J. W. G. Wildöer, L. C. Venema, A. G. Rinzler, R. E. Smalley and C. Dekker, Nature **391**, 59 (1998).
54. T. W. Odom, J. L. Huang, P. Kim and C. M. Lieber, Nature **391**, 62 (1998).
55. M. Ouyang, J. L. Huang, and C. M. Lieber, Phys. Rev. Lett. **88**, 066804 (2002).
56. D. D. D. Ma, C. S. Lee, F. C. K. Au, S. Y. Tong, S. T. Lee, Science **299**, 1874 (2003).
57. Z. Gai, H. Yu, and W. S. Yang, Phys. Rev. **B53**, 13547 (1996).
58. Z. Gai, R. G. Zhao, and W. S. Yang, Phys. Rev. **B56**, 12303 (1997).
59. R. J. Hamers, R. M. Tromp, and J. E. Demuth, Phys. Rev. Lett. **56**, 1972 (1986).
60. R. J. Hamers, Ann. Rev. Phys. Chem. **40**, 531(1989).
61. R. C. Jaklevic and J. Lambe, Phys. Rev. Lett. **17**, 1139 (1966).
62. B. C. Stipe, M. A. Rezaei, W. Ho, Science **280**, 1732 (1998).
63. L. J. Lauhon and W. Ho, Phys. Rev. **B60**, R8525 (1999).
64. K. Wandelt, in "Thin Metal Film and Gas Chemisorption", edited by P. Wissmann (Elsevier, Amsterdam, 1987).

65. J. F. Jia, K. Inoue and Y. Hasegawa, W. S. Yang, T. Sakurai, Phys. Rev **B58**, 1193 (1998).
66. G. Binnig, N. Garcia, H. Rohrer, J. M. Soler, F. Flores, Phys. Rev. **B30**, 4816 (1984); J. Tersoff, and D. R. Hamann, Phys. Rev. Lett. **50**, 1998 (1983).
67. G. Binnig, H. Rohrer, Surf. Sci. **126**, 236 (1983).
68. Y. Hasegawa, J. F. Jia, K. Inoue, A. Sakai, T. Sakurai, Surf. Sci. **386**, 328 (1997).
69. J. F. Jia, K. Inoue and Y. Hasegawa, W. S. Yang, T. Sakurai, J. Vac. Sci. Technol. **B15**, 1861 (1997).
70. K. Besocke, B. Krahl-Urban, H. Wagner, Surf. Sci. **68**, 39 (1977); B. Krahl-Urban, E. A. Niekisch, H. Wagner, Surf. Sci. **64**, 52 (1977).
71. R. Smoluchowski, Phys. Rev. **60**, 661 (1941).
72. G. Binnig and H. Rohrer, IBM J. Res. Dev. **30**, 355 (1986).
73. Y. Hasegawa, J. F. Jia, T. Sakurai, Z. Q. Li, K. Ohno, and Y. Kawazoe, in "Advances in scanning probe microscopy", edited by T. Sakurai and Y. Watanabe, Springer, 2000, p. 167.
74. D. M. Eigler, and E. K. Schweizer, Nature **344**, 524 (1990).
75. M. A. McCord, and R. F. W. Pease, Appl. Phys. Lett. **50**, 569 (1987).
76. J. A. Dagata, J. Schneir, H. H. Harary, J. Bennett and W. Tseng, J. Vac. Sci. Technol. **B9**, 1384 (1991).
77. G. Dujardin, R. E. Walkup, and Ph. Avouris, Science **255**, 1232 (1992).
78. S. T. Yau, D. Saltz, M. H. Nayfeh, Appl. Phys. Lett. **57**, 2913 (1990).
79. U. Staufer, R. Wiesendanger, L. Eng, L. Rosenthaler, H. R. Hidber, H.-J. Güntherodt, and N. García, Appl. Phys. Lett. **51**, 244 (1987).
80. M. F. Crommie, C. P. Lutz and D. M Eigler, Science **262**, 218 (1993).
81. H. C. Manoharan, C. P. Lutz, D. Eigler, Nature **403**, 512 (2000).
82. B. C. Stipe, M. A. Rezaei, W. Ho, S. Gao, M. Persson, and B. I. Lundqvist, Phys. Rev. Lett. **78**, 4410 (1997).
83. S.-W. Hla, L. Bartels, G. Meyer, and K.-H. Rieder, Phys. Rev. Lett. **85**, 2777 (2000).
84. F. Moresco, G. Meyer, K.-H. Rieder, H. Tang, A. Gourdon, and C. Joachim, Phys. Rev. Lett. **86**, 672 (2001).
85. D. T. Pierce, Phys. Scr. **38**, 291 (1988).
86. M. Bode, Rep. Prog. Phys. **66**, 523 (2003).
87. R. Wiesendanger, H.-J. Güntherodt, G. Güntherodt, R. J. Gambino, and R. Ruf, Phys. Rev. Lett. **65**, 247 (1990).
88. R. Wiesendanger, I. V. Shvets, D. Bürgler, G. Tarrach, H.-J. Güntherodt, and J. M. D. Coey, Z. Phys. **B86**, 1(1992).
89. R. Wiesendanger, I. V. Shvets, D. Bürgler, G. Tarrach, H.-J. Güntherodt, J. M. D. Coey and S. Gräser, Science **255**, 583 (1992).
90. S. Heinze, M. Bode, A. Kubetzka, O. Pietzsch, X. Nie, S. Blügel, R. Wiesendanger, Science **288**, 1805 (2000).
91. Kubetzka, M. Bode, O. Pietzsch, and R. Wiesendanger, Phys. Rev. Lett. **88**, 057201 (2002).
92. M. Bode, M. Getzlaff, and R. Wiesendanger, Phys. Rev. Lett. **81**, 4256 (1998).
93. W. Wulfhekel and J. Kirschner, Appl. Phys. Lett. **75** 1944 (1999).
94. S. H. Pan, E. W. Hudson, and J. C. Davis, Rev. Sci. Instrum. **70**, 1459 (1999).
95. B. I. Barker, S. K. Dutta, C. Lupien, P. L. McEuen, N. Kikugawa, Y. Maeno, J. C. Davis, Physica **B329–333**, 1334 (2003).
96. Q. Niu, C. Chang, C. K. Shih, Phys. Rev. **B51**, 5502 (1995).
97. S. Tsukamoto, B. Siu, and N. Nakagiri, Rev. Sci. Instrum. **62**, 1767 (1991).
98. H. Watanabe, C. Manabe, T. Shigematsu, and M. Shimizu, Appl. Phys. Lett. **78**, 2928 (2001).
99. H. Grube, B. C. Harrison, J. F. Jia, and J. J. Boland, Rev. Sci. Instrum. **72**, 4388 (2001).
100. H. Okamoto and D. Chen, Rev. Sci. Instrum. **72**, 4398 (2001).
101. S. Hosaka, T. Hasegawa, S. Hosoki, and K. Takata, Rev. Sci. Instrum. **61**, 1342 (1990).
102. L. Kuipers, R. W. M. Loos, H. Neerings, J. ter Horst, G. J. Ruwiel, A. P. de Jongh, and J. W. M. Frenken, Rev. Sci. Instrum. **66**, 4557 (1995).
103. J. Wintterlin, J. Trost, S, Renisch, R. Schuster, T. Zambelli, G. Ertl, Surf. Sci. **394**, 159 (1997).
104. R. Curtis, M. Krueger, and Eric Ganz, Rev. Sci. Instrum. **65**, 3220 (1994).
105. R. Curtis, T. Mitsui, and E. Ganz, Rev. Sci. Instrum. **68**, 2790 (1997).
106. C. Y. Nakakura, V. M. Phanse, G. Zheng, G. Bannon, E. I. Altman, and K. P. Lee, Rev. Sci. Instrum. **69**, 3251 (1998).
107. D. Croft and S. Devasia, Rev. Sci. Instrum. **70**, 4600 (1999).
108. L. Petersen, M. Schunack, B. Schaefer, T. R. Linderoth, P. B. Rasmussen, P. T. Sprunger, E. Laegsgaard, I. Stensgaard, and F. Besenbacher, Rev. Sci. Instrum. **72**, 1438 (2001).

109. T. R. Linderoth, S. Horch, E. Lægsgaard, I. Stensgaard, and F. Besenbacher, Phys. Rev. Lett. **78**, 4978 (1997).
110. S. Horch, H. T. Lorensen, S. Helveg, E. Lægsgaard, I. Stensgaard, K. W. Jacobsen, J. K. Nørskov and F. Besenbacher, Nature **398**, 134 (1999).
111. J. Wintterlin, S. Völkening, T. V. W. Janssens, T. Zambelli, G. Ertl, Science **278**, 1931 (1997).
112. C. Sachs, M. Hildebrand, S. Völkening, J. Wintterlin, G. Ertl, Science **293**, 1635 (2001).
113. C. Sachs, M. Hildebrand, S. Völkening, J. Wintterlin, and G. Ertl, J. Chem. Phys. **116**, 5760 (2002).